NASA Reference Publication 1380

1995

SSM/I Sea Ice Concentrations Using the Bootstrap Algorithm

Josefino C. Comiso
Goddard Space Flight Center
Greenbelt, Maryland

National Aeronautics and Space Administration

Goddard Space Flight Center
Greenbelt, Maryland 20771
1995

This publication is available from the NASA Center for AeroSpace Information,
800 Elkridge Landing Road, Linthicum Heights, MD 21090-2934, (301) 621-0390.

TABLE OF CONTENTS:

1. INTRODUCTION

One of the most important polar ocean parameters provided by satellite passive-microwave data is sea ice concentration. Ice-concentration maps are used to estimate ice extent, actual ice area, and the amount of open water within the ice pack. They are also needed in the calculation of heat, humidity, and salinity fluxes between the ocean and the atmosphere; in the monitoring of occurrences, impact, and persistence of polynyas; and in estimating meltwater production during spring and summer months. Also, these data are invaluable in many commercial, navigational, and operational applications.

Several techniques have been developed to obtain ice concentration from passive-microwave data (Svendsen et al., 1983; Cavalieri et al., 1984; Swift et al., 1985; Comiso, 1986; Comiso and Sullivan, 1986; Gloersen and Cavalieri, 1986; Cavalieri et al., 1991). A review of these techniques and a comparison of some ice-concentration results is presented by Steffen et al.(1992). Although the various techniques provide approximately consistent location of the ice edges, there are differences in the derived fraction of open water within the ice pack, partly because of the use of different sets of Special Sensor Microwave Imager (SSM/I) channels. Differences as large as 20% in areas like the Bellingshausen/Amundsen Seas have been noted by Comiso et al. (1992).

Evaluation of algorithms is difficult because of the lack of good validation data sets. Comparative studies with limited Landsat images provide useful information but cannot always be used to resolve the discrepancies because such images are usually not available where and when the differences are largest, especially in midwinter. Comparative analysis of Advanced Very High Resolution Radiometer (AVHRR) ice concentrations with results from both NASA Team and Bootstrap algorithms have been done by Emery et al. (1994) mainly for the summer period when errors are known to be large. Also, it is not clear that AVHRR can be used for validation purposes since the resolution is crude (>1 km) compared to the size of the ice features during winter and summer. Also, ice concentrations derived from the summer data may have large errors because the surface undergoes changes in albedo at this time because of melt and meltponding and because of imperfect cloud masking. Furthermore, summertime is when the passive-microwave algorithms have the largest uncertainties because of largely varying emissivities. Comparative analysis with Synthetic Aperture Radar (SAR) data may provide further insights into the

actual state of the Arctic ice cover because of its all weather capabilities and its high resolution, which enable discrimination of surface features. Unsupervised extraction of ice concentration from SAR is only possible during the summer when wind speed is greater than 4 m/sec. Otherwise, supervised classification must be used and errors are larger.

In this paper, a detailed discussion of the Bootstrap algorithm as implemented for the SSM/I data is presented. Also, the basic principles and the physics behind the algorithm, as well as the basis for making changes when SSM/I data instead of data from the Scanning Multichannel Microwave Radiometer (SSMR) are used, will be discussed. Some results from ground and aircraft radiometer measurements are also presented to support the basis for the technique. Finally, systematic and statistical errors are evaluated. Because of the lack of an adequate validation data set, the absolute values of ice concentration are difficult to establish. However, some assumptions can be made regarding the ice cover that enables a first-order estimate of the errors.

This work was supported by the Cryosphere Program at NASA Headquarters. The programming supports from Rico Allegrino of Hughes STX and Larry Stocks of Caelum Inc. are very much appreciated.

2. THE BOOTSTRAP ALGORITHM

2.1 The Basic Technique

The basic radiative transfer equation that expresses the brightness temperatures in terms of surface emission and accounts for atmospheric and other effects is given by

$$T_B = \varepsilon T_S e^{(-\tau)} + T_U + (1-\varepsilon) T_D e^{(-\tau)} + (1-\varepsilon) T_s e^{(-2\tau)} \qquad (1)$$

where τ is the atmospheric opacity, ε is the surface emissivity, T_S is the surface physical temperature, T_U is the atmospheric upwelling radiation, T_D is the atmospheric downwelling component of radiation, and T_s is the cosmic background component. The first term in equation (1) is the dominant term that provides the surface information of interest, while the other terms are contributions from the atmosphere and outer space. Ice concentration is usually derived using a mixing formulation that considers two (or three) types of surfaces, namely ice (first-year and multiyear) and open water. In the algorithms by Swift et al. (1985) and Svendsen et al. (1983),

atmospheric effects are accounted for by making use of equation (1) in conjunction with measured atmospheric profiles in specific areas at specific times. Their scheme is normally effective in the areas where such atmospheric parameters are available. However, it is not so effective in areas where atmospheric profiles are not available. In the scheme by Cavalieri et al. (1984), spatial changes in surface temperature are accounted for by the use of polarization and gradient ratios. In the one-channel algorithm used by Zwally et al. (1983) and Parkinson et al. (1987), the reference brightness temperatures of open water were derived indirectly from histograms of brightness temperatures over ocean, and the expected changes in physical temperature were accounted for by the use of climatological surface temperatures. There are, however, spatial changes in the emissivity of the ice surface that also need to be accounted for in these algorithms.

The Bootstrap technique for ice-concentration determination was originally developed separately for the Antarctic (Comiso et al., 1984; and Comiso and Sullivan, 1986) and the Arctic (Comiso, 1986). The Bootstrap algorithm takes advantage of the multichannel capability of the SMMR and SSM/I sensors to obtain the appropriate reference brightness temperature for each data element. To gain insight into this capability, scatter plots of SSM/I winter data (a weekly average from March 9 to March 15, 1988) in 3-D using (a) 19V vs. 37V vs. 37H and (b) 19V vs. 85V vs. 37V are presented in Figure 1. Two-dimensional components of each pair of channels are also shown. In these plots, data points from the Arctic inside a rectangular area with corner points at (60°N, 180°W), (60°N, 90°E), (60°N, 90°W), and (60°N, 0°) were studied and observed to form clusters labeled A, B, C, and D. In winter, ice surfaces represented by each of these data points are expected to be near 100% ice concentration. Generally, the different clusters do not fall along the same line, especially in the set of channels shown in Figure 1(b). The nonlinearity and the large variability in brightness temperature are caused primarily by scattering of emitted radiation within the ice. Different types of ice (or snow) surfaces have different scattering properties, especially at different wavelengths (or frequencies).

A most welcomed feature of the cluster plots is the high correlation between the 37H and 37V GHz channels. The 2-D component of the 3-D plot in Figure 1(a) is replotted in Figure 2(a). This set of channels is found useful for the ice-concentration algorithm because (a) it provides the best resolution

from the set of channels (i.e., 19 GHz and 37 GHz at both polarizations) currently used for ice algorithms; (b) the standard deviation across the linear cluster is less than ± 2.5 K and may provide the precision suitable for the Arctic region where the percentage of open water is usually less than 5% in winter; (c) surface temperature variations are approximately taken into account; and (d) the slope of the line AD, which is used to find the tie-point for consolidated ice, is consistently close to 1.0 in every winter data set from either SMMR or SSM/I. The set, which we will call HV37, is especially suitable for the Central Arctic region during the winter period. In the other regions, the set of channels consisting of the vertically polarized 19 GHz and 37 GHz data are utilized instead, because the horizontally polarized data appear to be highly variable in these regions and provide relatively higher retrieval errors. The latter set will be called V1937. For convenience, the set of vertically polarized 18 GHz and 37 GHz data used for SMMR will be called V1837.

Using a mixing formulation, the ice concentration, C_B, can be estimated from a single channel measurement T_B using the equation

$$C_B = (T_B - T_O)/(T_I - T_O) \qquad (2)$$

where T_O and T_I are reference brightness temperatures of open water and of 100% ice, respectively. This assumes that T_O and T_I are the appropriate values for the particular sample. Because of spatial variability in the emissivity and physical temperature of sea ice, these reference temperatures are not constant. The algorithm uses two channels to determine the reference temperatures as described below.

The line AD in the HV37 scatter in Figure 2(a) can be parametrized to determine T_I in equation (2). The actual slope and offset of the line AD are inferred from the scatter plot, as will be described later. A schematic of the technique is shown in Figure 3. In the diagram, data points along the line AD correspond to 100% ice surfaces, with different emissivities and/or temperatures. Some of these data points may represent pure ice types, while others may represent mixtures of different types. In the formulation, a data point at location I may be thought of as representing 100% ice cover of a certain ice type with specific emissivity and temperature. Data points along the line OI thus represent different concentrations of this ice type.

Following equation (2), the ice concentration varies linearly along this line, as indicated in the diagram. The algorithm is effective as long as most of the 100%-ice data points fall approximately along the line AD. As will be discussed later, 100% new-ice data points may not fall along this line because the emissivities of new ice are lower than those of thick ice (Comiso et al., 1992). Atmospheric effects are automatically accounted for approximately in this formulation, because the atmospheric terms are already included in the observed satellite data as described in Zwally et al. (1983).

The location of I for a given brightness temperature, T_B, located at the data point B, is determined by finding the common values (intercept) of two linear equations corresponding to the two lines AD and OB. More explicitly, the equations for AD and OB can be expressed, respectively, as follows:

$$T_{1I} = T_{1A} + (T_{2I} - T_{2A})(T_{1A}-T_{1D})/(T_{2A} - T_{2D}) \quad (3)$$

$$T_{1I} = T_{1O} + (T_{2I} - T_{2O})(T_{1B}-T_{1O})/(T_{2B} - T_{2O}) \quad (4)$$

where T_{1I} and T_{2I} are the temperature coordinates at the intercept, and the prefixes 1 and 2 correspond to channels 37H and 37V, respectively, in the HV37 set and to channels 19V and 37V in the V1937 set. The other variables are the set of brightness temperature values for A and D, which can be any two points along the line AD, T_O, which is constant and inferred from the data, and T_B, which is the input data. The reference temperature for open water is derived from the scatter plot (or frequency histograms from each channel) as follows. The cluster of points along the line OW in Figure 1(a) represent data in the open ocean region with data points closer to W representing surfaces under stormy weather conditions. Inside the ice pack, open water normally has a smooth surface, because many of the wave effects have been attenuated by ice floes. The reference temperature for open water therefore is taken as that close to the lowest open ocean value (i.e., near where lines OA and OW intersect). Ice concentration for any data point at B can be derived from equation (2) using either of the sets of channels. However, there is a singularity whenever $T_I = T_O$. This can be avoided by using corresponding values from the other channel. The ratio of the distances OB and OI provides the same answer and has no singularity.

Using equations (3) and (4) and values at O and B, the intercepts can be calculated as follows:

$$T_{1I} = (T_{1A} - T_{1O} - T_{2A}S_{AD} + T_{2O}S_{OB})S_{OB}/(S_{OB} - S_{AD}) + T_{10} - S_{OB}T_{20} \quad (5)$$

$$T_{2I} = (T_{1A} - T_{1O} - T_{2A}S_{AD} + T_{2O}S_{OB})/(S_{OB}-S_{AD}) \quad (6)$$

where S_{AD} and S_{OB} are slopes of the lines AD and OB, respectively. The ice concentration, C, can thus be derived from the ratio using the equation

$$C = [\{(T_{1B}-T_{1O})^2+(T_{2B}-T_{2O})^2\}/\{(T_{2I}-T_{2O})^2 + (T_{1I}-T_{1O})^2\}]^{1/2} \quad (7)$$

This ratio was adapted for use in the Bootstrap Algorithm because it is easier to parametrize, and it provides generally better statistical accuracy than the sole use of either channel. A sample basic program that calculates ice concentration for a given set of brightness temperatures is provided in Appendix A. In the formulation, T_{2A} and T_{1A} may be taken as the coordinates of any point along the line. By choosing $T_{2A} = 0$, T_{1A} would become the offset, as given in Table 1.

In the entire Antarctic region and in some regions of the Arctic, the V1937 set is used. The reason for this is that empirical analysis indicated that the use of the 18 GHz (V) versus the 37 GHz (V) set (using SMMR) provides temporally and spatially more coherent values than the HV37 set (Comiso et al., 1984; Comiso and Sullivan, 1986). This is partly because the sensor angle of incidence is near the Brewster angle where the brightness temperature for ice at vertical polarization is much more stable than that at horizontal polarization. In the Antarctic and the Arctic seasonal ice regions, the ice cover consists mainly of first-year ice, the emissivity of which is expected to be more uniform than those in the Central Arctic and affected mainly by surface and snow-cover effects. The data points in these areas, therefore, are not as much affected by volume scattering within the ice and do not usually form the nonlinear ice clusters observed in the perennial ice region. A sample scatter plot in the Antarctic region is shown in Figure 2a. In Comiso and Sullivan (1986), it was observed that some SMMR data points along AD in the V1937 set would fall below the AD line in the HV37 set causing the ice concentration to

be considerably lower when the latter set is used. A similar phenomenon is observed from the SSM/I data. The physics behind this apparent inconsistency are not very well understood, but the polarization of sea ice has been observed to be sensitive to ice layering, roughness effects, snow wetness and flooding (Matzler et al., 1984). Such conditions have been observed to be common in many areas of the ice pack (Tucker et al., 1992).

2.2. Choice of Tie-Points

The reference brightness temperatures (called tie-points) for ice (T_I) and open water (T_O) are determined from the scatter plots of actual satellite data such as those shown previously. In a sense, the algorithm is called Bootstrap, because the technique is based on the distribution of actual data points. As explained previously, the 100%-ice tie-point is along the line AD in Figure 3. The line AD is drawn parallel to the cluster of points but slightly above the centroid of the linear cluster, as discussed below. The same line is used to process all SSM/I winter data (e.g., late October through early June) for all years. Adjustments are made during spring melt, midsummer, and early autumn, to account for changes in surface emissivity during these periods. The tie-points for open water within the ice pack are also inferred from data points of ice-free ocean, which can be identified in the scatter plots as described earlier.

The choice of tie-points is shown more quantitatively in the frequency histogram shown in Figure 4. The data in the histogram are binned such that the distance between the ocean tie-point and the line AD (i.e., OI) is constant. Thus, the abscissa is basically in a normalized unit that is directly convertible to ice concentration. The width of the peak at the brightness temperature value of around 255 K represents the scatter of data points across the line AD in the V1937 set. The line AD is positioned in such a way that it is approximately at the location, indicated by the arrow A (approximately the peak plus the half width at half height), and close to the inflection point. The tie-point for open water is similarly determined and indicated by the arrow labelled O. In the latter case, the tie-point is about two standard deviations below the water peak. This is approximately where the lines OA and OW intersect.

The slopes and offsets used as reference for consolidated ice in the algorithm are given in Table 1. Also, in Table 1 are tie-points for open water

in both hemispheres and for cold (winter) and warm (summer) periods. The source of errors associated with these values is discussed in the next section. The values used in creating previous editions of Bootstrap Compact Disk-Read Only Memory (CD-ROM) ice concentrations are given in Table 2. The new values in Table 1 provide ice concentrations that are only slightly different (about 1.5% on the average) from those in Table 2 during the winter period and are based on March and September 1992 data for the Arctic and the Antarctic regions, respectively. The values in Table 2 were derived from March and September 1988 for the Arctic and Antarctic regions, respectively. The key difference between the two tables are the tie-points for the summer period in which adjustments were made in Table 1 to better match ice concentrations derived from SAR (Comiso and Kwok, 1993). The winter values were kept constant because of aforementioned stability in the signatures during the period (see Figures 5 and 6). When moving from one set of channels to another (i.e., HV37 to V1937), it is important to ensure that the reference points are properly matched. The slopes and offsets have been adjusted so that both sets of channels provide approximately the same ice concentrations for most data points.

2.3. Special Considerations

In the formulation, it would be desirable to have all data points fall within the triangle ADO as shown in Figure 3. With the SSM/I data, some of the data points fall outside this triangle because of random noise and spatial variations in physical temperatures and emissivities. A special problem arises for data points to the right of the line OA. Most of these data points are from surfaces covered by new ice, especially pancakes near the marginal ice zone. These data points could lead to a very long segment OI if the aforementioned technique for determining I is used. For example, in Figure 3, if the data point is at "X," the line OI would be about twice the length of OA. However, the peak emissivity is supposedly represented by a data point near A, and the length of the segment OA is supposed to be close to the upper limit of OI. To minimize errors associated with abnormally large OIs, ice concentrations for data points below the line OA are derived by replacing OI with OA. The data affected by this consideration is a very small fraction of the total ice data in the Arctic. The scheme, however, provides more realistic values for these data points.

The HV37 set is used only in the northern hemisphere and primarily in the Central Arctic. Because of the aforementioned potential problems with polarization, the HV37 set is used only for data points above the line AD - 5 K, with the rest of the hemisphere using the V1937 set. The idea is to use the HV37 set of channels only in the primarily multiyear ice (or perennial) region where the nonlinearity in the cluster of points in this region in the V1937 set affects the calculation of ice concentration. The -5-K offset was used to include data with about 5% to 10% open water, which is typical in the Arctic region during winter. In an older version of the program, data points within 14 K of A (inside the sector with radius S in Figure 3) were excluded in the 37H vs. 37V analysis for the same reason. In this concept, data points inside the circle (shaded area) were analyzed using the V1937 set to get most of the seasonal ice-cover data analyzed with this set of data. The locations of A used for this purpose are given in Table 3. This option has been removed because removal provided basically the same ice-concentration results and simplified the algorithm.

To provide an idea about which set is used in the various regions of the Arctic, the geographic location of pixels using the HV37 set on January 15 and on May 15, 1992 are shown in Figure 7, (a) and (b), respectively. It is apparent that in winter (i.e., January), the HV37 set was used for much of the Arctic while in spring (i.e., May), the area where it is used is more confined to the Central Arctic Region. Statistically, during a 3-month period from January through March and from April through June, the percentages of data points that use the HV37 set for each data element are shown in Figure 8, (a) and (b), respectively. Again, high percentages in the winter, especially in the Central Arctic, indicate that the HV37 set is heavily utilized. In the late spring and summer, the HV37 set lost its distinct signature in the perennial ice region because of surface wetness and meltponding effects. At this time, the use of the HV37 set is no longer as important as in winter because volume scattering and temperature effects are minimal.

2.4. Open Ocean Mask

In some areas of the open ocean, atmospheric effects, big waves, higher temperatures, and foam cause the brightness temperatures to increase substantially. Application of the algorithm in these areas produces unrealistic ice-concentration values. Fortunately, in scatter plots of two or

more channels, data points from the open-ocean regions are clustered along a line (e.g., OW in Figure 1) that can be isolated from those in ice-covered areas. An ocean mask that utilized a threshold using the V1837 set was applied in Comiso et al. (1984) but was first documented in Comiso and Sullivan (1986). With SSM/I data, the same method was applied, but not as effectively, because the sensor uses 19.35 GHz, which is closer to the water vapor line (22 GHz) than the 18 GHz used in SMMR. The effect was to make it more difficult to discriminate some open-ocean areas from those with ice cover. To overcome much of the problem, the original technique is still utilized, except that instead of using the V1937 set, the 22 GHz channel at vertical polarization is substituted for 37 GHz as shown in Figure 9(a). The scheme automatically sets data points below the line in Figure 9(a) to 0%. However, an addition mask is added to take care of extreme atmospheric conditions. Data above a certain threshold, M_0 as indicated in Table 1 for the difference of 22 GHz and 19 GHz data (i.e., $T_{22V} - T_{19V}$), is also set to 0%. Because the signatures of data along the line AW vary with location during the year, some seasonal adjustments for the threshold values are made, as shown in Table 1.

2.5. Ocean/Land Boundary Mask

The ice-concentration maps generated by the algorithm also show relatively high ice concentrations in coastlines that are known to be ice free in recent times (e.g, Great Britain, Spain, and the western coast of Alaska). Because of large footprint, brightness temperatures along these coastlines represent measurements of mixtures of land and ocean which unfortunately are similar to those of mixtures of ice and water. There is also further contamination caused by antenna side lobes that give different values as the satellite crosses the land/ocean boundary from different directions. A masking technique similar to that used for open ocean and ice would be desirable, but the search for a set of channels that could do the masking consistently and effectively has not been successful. To illustrate the problem, scatter plots using different sets of channels (Figure 10) show that data points along the land/ocean boundaries (represented by x) are randomly distributed along the line OA, making it difficult to discriminate these points from those of partially ice covered surfaces. While an unsupervised technique that works has not been developed, an ocean/land boundary mask based on visual inspection of the location of the ice cover has been used. The latter is done primarily with weekly 85 GHz data

which show little contamination because of higher resolution and AVHRR data, when available. This mask applies to land/ocean boundaries where ice floes have not been observed in recent times and also where ice has retreated from during the summer. This is an important enhancement in the generation of ice-concentration maps, because its use minimizes errors in the calculation of some of the ice-climate parameters, such as ice extent and actual ice area.

3. ERROR ANALYSIS

Several field and aircraft experiments have been performed in both polar regions to study the basic assumptions used in the algorithm. The existence of large areas of 100% ice cover in both hemispheres has been verified with aircraft, helicopter, and ship measurements. Figure 11, (a) and (b), shows scatter plots of data taken by the Airborne Multichannel Microwave Radiometer (AMMR) onboard the NASA P3 aircraft over the Arctic region in May 1987 as reported by Comiso et al. (1991). The data points clustered along the line AD in both HV37 and V1837 sets have been established to correspond primarily to >95% ice cover using coincident photography, SAR, and visual observations. Despite a smaller footprint size of about 1 km for the aircraft data, compared to 25 km for satellite data, the data points are basically linear and well defined. Data over the same general area, but at a much higher resolution (58 m), show the same patterns but more scatter of data points, because the emissivities of individual features (which are more variable) are better represented. Good consistency of radiometer ship measurements (e.g., Comiso et al., 1989) with these patterns was also observed. Such sets of data thus provide a good empirical basis for the assumption that a line parallel to AD can be used as reference brightness temperatures for 100% ice, as done in the Bootstrap algorithm.

Validation of derived ice concentrations from passive-microwave data is difficult for many reasons. The ice cover is vast, and during winter, it is usually in darkness. Field data observed from ships are difficult to use for verification purposes because of possible mismatches in observations. For example, it would take several hours or days of ship time to produce visual observations that would match the instantaneous value observed from a 25- by 25-km area by the sensor. Aircraft data are generally more useful because of better spatial coverage, good resolution, and availability of ancillary measurements, but they also need to be validated by ground measurements. The

other strategy has been to utilize high-resolution satellite (or space-shuttle) data for validation. The use of high-resolution data has its advantages, but such a strategy degenerates into comparative analysis, because these other satellite data also need to be validated. For example, unambiguous discrimination of open water, grease ice, small pancakes, and gray nilas in both visible and microwave channels may be impossible even with high-resolution sensors. Nevertheless, data from such sensors are useful in setting up lower limits in ice concentrations. Although an appropriate validation data set is difficult to obtain, it is also fortuitous that the ice concentration of a large fraction of the inner pack has been observed to be close to 100% ice. This helps in the search for the locations of 100% ice cover that can be used to establish the validity of the reference temperatures used by the algorithm.

3.1. New Ice and the Ice Margin

Consistent averages of ice-edge conditions are provided by the passive-microwave data. However, the derived ice-concentration gradients at the ice edge are generally broad and several pixels wide. Although such gradients are possible, especially during storms or ice retreat, field observations have indicated a shorter distance from the ice edge to the inner pack. The ice gradient provided by the satellite may be affected by the nature of the antenna pattern of the sensor, which makes precise gridding of the data difficult, and the side lobes, which tend to smear the ice edges because of inconsistencies in the measurements of the same ice edge as the satellite passes by from different directions. Another factor that affects the measurement of the gradient is the abundance of new ice in the region (especially grease ice and pancakes of different sizes and thicknesses), the concentration of which is usually underestimated in the algorithm, because the emissivities of such ice types are generally lower than those of thick ice (Comiso et al., 1992).

In the inner pack, the quantification of open water is also complicated by the transient nature of the surface. Open water in newly formed leads, for example, seldom stays open for a long time. In a matter of a few hours, the open water is covered by grease ice that tranforms into nilas and then young ice. During this transition period, the emissivity of the surface is constantly changing, as discussed in Grenfell and Comiso (1986). In predominantly new-ice areas, the use of the regular tie-point (based on AD) could cause as much as 30% error in the retrieval (Comiso et al., 1992).

However, in much of the inner pack, the fraction of new ice/open water is small, and the net effect on estimates of ice concentration is generally minimal.

Having this error in the retrieval of new ice is not necessarily all negative. The error provides a means to detect large areas of divergence, polynyas, and the conditions of the marginal ice zones. Because of subfreezing temperatures in these regions, new ice forms almost immediately, except in sensible heat polynyas. Also, heat flux calculations would be more accurate if large areas of new-ice are identified even in terms of concentration values that are lower than average.

3.2 Spatial Changes in Physical Temperature

Even in areas where the emissivity is relatively uniform, errors in the calculation of ice concentration can be caused by changes in the physical temperatures of the emitting layer. The sensitivity of the brightness temperatures to 15-K and 30-K spatial changes in the physical temperature is illustrated in Figure 2, (c) and (e), respectively, for the HV37 set and (d) and (f) for the V1937 set. In the HV37 case, variations in the temperature of the emitting ice layer are shown to cause almost negligible effect on the width of the cluster distribution. This is mainly because the slope of the ice line happens to be approximately 1, and the depths (and hence temperatures) of the emitting layer at both polarizations are about equal. In the V1937 case, the sensitivity to temperature is significantly greater as shown in Figure 2(d) and (f) because the slope of the line AD is between 0.47 to 0.58 instead of 1.

The changes in ice concentration associated with each Kelvin change in physical temperature are given in Table 4 for both the V1937 sets and the HV37 set. In the HV37 set, the ice concentration change is 0.05% for each Kelvin change in the ice temperature, while in the V1937 set, the change is about 0.91% in the Antarctic and 0.84% in the Arctic. However, in the seasonal ice region where the V1937 set is utilized, it has been observed (i.e., Weddell and Ross Seas) that the fluctuation of the temperature of the emitting layer is small because the snow layer provides such a good insulation. In the Ross Sea ice pack, the snow-ice interface temperature was found to be virtually independent of short-term fluctuations of air temperatures when the snow layer was at least 10 cm thick (M. Jeffries, private communications, 1995). Such results are also reflected during a 3-day ice experiment over a large ice floe

in the inner pack of the Weddell Sea in 1989 (Figure 12). In eight camp sites where the snow thickness varied from 15 to 31 cm, the snow-ice temperature changed by only 1 to 2 Kelvins, while the air temperature fluctuated by as much as 20 K. During a 6-month period in 1986, almost daily observations in the Weddell Sea region also indicated very little fluctuation in the snow-ice temperature. An average of -6 ^{o}C was observed with a standard deviation of about 2 K (Comiso et al., 1989). The lowest snow-ice interface temperature measurement recorded was -12 ^{o}C, which deviates from the average by only about 6 K. Sample conversions of surface-air temperatures to snow-ice temperatures are given in Table 5. Three methods are utilized: one using regression results from 3 months of data taken in the Weddell Sea in 1986; another using regression results from several years of data from Pond Inlet in the Arctic (Ramseier, private communications, 1981); and the last using the 25% rule described in Zwally et al., (1983). In the Antarctic and most of the other seasonal regions, the results of Comiso et al. (1989) are believed to be most appropriate. The result is supported by numerical estimates (e.g., Parkinson, private communication, 1995), which indicate that for an average thickness of 75 cm (Wadhams, et al., 1987), and an average snow cover of 20 cm, the snow-ice interface temperature is the water temperature plus 64% of the difference (versus 25% used by Zwally et al., 1983) between surface-air temperature and water temperature at the bottom of the ice. The estimate was for fresh snow with conductivity of 3 W $m^{-1}K^{-1}$ and density of 200 gm/cm^3. Using higher conductivity and density values, which may be more typical for snow cover over sea ice, the estimate of 64% becomes 55%. The snow-ice interface temperatures corresponding to both 64% and 55% are also shown in Table 5. Both show good consistency with the 1986 Weddell observations.

To gain additional insight into the effect of temperature change to the ice-concentration estimates, Figure 13, (a) and (b), shows V1937 scatter plots of data points in the Antarctic region for May 11 and September 19, 1992, respectively. The reference brightness temperatures used by the algorithm for 100% ice cover are inferred from the line AD in the plot, as discussed earlier. The corresponding ice-concentration maps that show only data points above the line AD-10 K are shown in Figure 14. Both images indicate that a dominant fraction of the Antarctic ice cover (including some continental coast lines) is included in this range. Assuming a fixed emissivity of 0.95 for ice, a change

of 10 K in brightness temperature corresponds to a change of 10.5 K in snow-ice interface temperature or a 9.5% change in ice concentration, using Table 5. Since the variability of data points includes actual changes in ice concentration, the variability of the snow-ice temperature is likely much less than 10.5 K, as indicated earlier.

Large fluctuations in surface-air temperatures in the inner pack of the Antarctic sea ice have been observed, but corresponding fluctuations in the snow-ice interface temperatures are suppressed because of the presence of snow. The results above indicate that most of the concentration values in the Antarctic region are basically 90% and above. Among the exceptions are the marginal ice zones and a few coastal regions, expecially where coastal polynyas and icebergs are located. Scatter plots of data points from the outer and inner zones of the Antarctic ice cover are shown in Figure 15, (a) and (b), respectively. In (a), data points in the outer zone of the Weddell Sea are plotted with those near the line AD being interpreted by the algorithm as having ice concentrations near 100%. Despite much lower surface temperatures expected in the inner zone, most of the data points, as shown in (b), are along or near the line AD. The same phenomenon is true with the data from the Ross Sea, Amundsen Sea, and Bellingshausen Sea, shown in (c) and (d). In the latter, some data points are along the line AO, but most of these correspond to data from the Ross Sea coastal polynya region.

3.3 Spatial Changes in Emissivity

Constantly changing emissivity of some surfaces is an unresolved problem. We already mentioned the case of new ice in winter in which the emissivity changes constantly as the surface goes through a metamorphosis from grease ice to nilas to young ice and then to first-year ice with snow cover. Even for thick first-year ice, the effective emissivity could change spatially because of differences in thickness and granularity of the snow cover, changes in surface wetness, flooding, and ridging (or rafting). Thick ice also usually has thick snow cover, partly because it has had the longest history, and was already there when there was a previous snow storm or snow transport through wind effects. Thick snow cover makes the free board closer to sea level and, therefore, makes the ice floe more vulnerable to flooding. The latter causes the formation of snow-ice at the ice interface, thereby altering the radiative characteristics of the material. Fortunately, in the Arctic where HV37 set is

utilized, the spatial variations in emissivity at 37 GHz (V) are highly correlated to those at 37 GHz (H). In other regions where the V1937 set is utilized, the ice cover is generally opaque and affected mainly by spatial changes in the characteristics of the snow cover. Errors in ice concentration caused by each Kelvin change in brightness temperatures of each data point and also of the tie-points are given in Table 4.

In spring and summer, the emissivity of thick ice also changes with time, especially over the perennial ice region in the Arctic. The slopes and offsets of the line AD (Figure 3) in the HV37 set are adjusted to take this into account automatically from onset of spring in June, through the meltponding period in July, August, and early September, to the freeze-up period in October at which time they are reset to the winter values. Despite this adjustment, the error can still be substantial, especially when there is meltponding on the surface, because the emissivity of meltponds is the same as that of open water (Grenfell and Lohanick, 1985).

3.4. Variability of Reference Brightness Temperatures

Under ideal winter situations when only thick ice and open water are present, ice concentration can be derived with the Bootstrap technique and the HV37 set at a precision of less than 5%, based on standard deviations of the reference brightness temperatures used in the formulation. Errors are higher in regions where the V1937 set is utilized as reflected by higher standard deviations of data points across the consolidated ice cluster. Statistical errors can be inferred from ice-concentration histograms such as those shown in Figure 16. The peak on the right shows the distribution of ice concentrations in heavily ice-covered regions. The standard deviations for the peaks are about 4% and 6% for the May 11 and September 19 data, respectively. The relative location of 100% ice is also different for the two periods, because on May 11, the ice cover was still growing, while on September 19, the ice extent was close to the maximum.

A bias in the ice-concentration values is possible because of the qualitative nature in establishing the tie-points. The uncertainty in the offset of the line AD is difficult to establish because of the lack of an adequate validation data set. The standard deviation of the ice distribution shown in Figure 16 can be a useful guide for estimating the upper limit of such uncertainty. Also, while the slopes show seasonal and interannual consistency,

some days show slight shifts in the location of the peak and different patterns that may be associated with atmospheric effects or temporal changes in surface emissivity. As more information about the ice cover becomes available (e.g., with concurrent use of high-resolution satellite data), errors in the offset and slope of AD can be minimized. Quantitative estimates of the errors associated with each parameter used in equations (5) - (7) can be inferred using Table 4.

Regional variations in the average emissivity of sea ice is also apparent in the data set. The scatter plots shown in Figure 15, for example, show that the distribution of data points in the Weddell Sea area are slightly different from those in the Ross/Bellingshausen/Amundsen Seas. The accuracies in the retrieval can be improved by having regional tie-points.

4. SUMMARY AND FUTURE DIRECTIONS

A detailed description of the Bootstrap algorithm for sea ice as discussed previously in earlier publications is presented. The algorithm was developed initially for the Nimbus-7 SMMR data and has been enhanced to make it more suitable for the SSM/I data. The technique utilizes relationships of multichannel distributions of the data to derive geophysical parameters. The physical basis for the formulation is presented and shown to be consistent with microwave observations from ships and aircrafts. Two modes of retrieval are used: one using the 37-GHz channels at both polarizations and another using the 19-GHz and 37-GHz channels at vertical polarization. The first is used primarily in the Arctic region and provides statistical uncertainties of less than 5%. The second is used primarily in the Antarctic and some of the seasonal regions of the Arctic. The statistical uncertainty in the latter region is about 10% and is greater than the first, because it does not account for spatial changes in physical temperatures of the emitting ice layer as well. Large variabilities in emissivity, and meltponding effects during the summer, further degrade the accuracy to about 20% to 25% in some regions.

The algorithm provides ice-concentration values that are coherent spatially and temporally. The product is generally useful for large-scale studies of the ice cover because of the consistency of the retrieved values and the good temporal resolution. SSMI ice concentration data from 1987 through 1991 have been archived in CD-ROM format by National Snow and Ice Data Center (NSIDC) at the University of Colorado using input parameters given in Table 2.

A revised version that will include data up to 1995 is in preparation and will be released in the near future. The new data set incorporates the enhanced ocean masking procedure described in Section 2.4, and tie-points (slightly changed in winter but enhanced to obtain better agreement with SAR data in summer) given in Table 1. Future releases will also include an SMMR ice-concentration data set which will cover the period from 1978 through 1987 using a procedure consistent with that used for the SSM/I data.

Using basically the same technique, some improvements are possible, among which are as follows:

(a) use of local algorithms to improve accuracies in areas where the emissivity of ice is very different from average emissivities,

(b) use of surface temperature measurements (e.g., from AVHRR) to better account for spatial changes in surface temperatures,

(c) improved summer ice retrievals that would take into account meltponding and other effects,

(d) improved ocean masking that automatically adjust to seasonal variations in atmospherice and other effects,

(e) use of a more automated ocean/land boundary mask, and

(f) better utilization of all the channels, especially in detecting and accounting for atmospheric and wave effects at the marginal zones.

It should be emphasized that the algorithm described and the tie-points used are meant for global retrievals. The reader should be aware that gridded brightness temperatures are readily available from NSIDC in CD-ROM format. The algorithm described in this document can be enhanced as suggested above for improved accuracies, especially in local areas where other data sets are available. With the advent of data from more advanced satellite sensors (e.g., SAR, Along Track Scanning Radiometer (ATSR), Moderate-Resolution Imaging Spectrometer (MODIS), etc...) the synergistic use of the latter with passive-microwave data is also encouraged.

5. REFERENCES

Cavalieri, D. J., P. Gloersen, and W. J. Campbell, "Determination of sea ice parameters with the Nimbus 7 SMMR," *J. Geophys. Res.*, **89(D4)**, 5355-5369, 1984.

Cavalieri, D. J., J. P. Crawford, M. R. Drinkwater, M. R., D. T. Eppler, L. D. Farmer, R. R. Jentz, C. C. Wackerman, "Aircraft active and passive microwave validations of sea ice concentration from the DMSP SSM/I," *J. Geophys. Res.*, **96(C12)**, 21989-22008, 1991.

Comiso, J. C., "Sea ice effective microwave emissivities from satellite passive microwave and infrared observations," *J. Geophys. Res.*, **88(C12)**, 7686-7704, 1983.

Comiso, J. C., "Characteristics of Winter Sea Ice from Satellite Multi-spectral Microwave Observations," *J. Geophys. Rev.*, **91(C1)**, 975-994, 1986.

Comiso, J. C., "Arctic Multiyear ice Classification and Summer Ice Cover using Passive Microwave Satellite Data," *J. Geophys. Res.*, **95(C8)**, 13411-13593, 1990.

Comiso, J. C., and R. Kwok, "Summer Arctic ice concentration and characteristics from ERS1-SAR and SSM/I data," *Proceedings of the First ERS-1 Symposium: Space at the Service of our Environment, Cannes, France, 4-6 November 1992*, **ESA SP-359**, 367-372, 1993.

Comiso, J. C., and C. W. Sullivan, "Satellite Microwave and In-Situ Observations of the Weddell Sea Ice Cover and its Marginal Ice Zone," *J. Geophys. Res.*, **91(C8)**, 9663-9681, 1986.

Comiso, J. C., S. F. Ackley, and A. L. Gordon, "Antarctic Sea Ice Microwave Signature and their Correlation with In-Situ Ice Observations," *J. Geophys. Res.*, **89(C1)**, 662-672, 1984.

Comiso, J. C., T. C. Grenfell, D. L. Bell, M. A. Lange, and S. F. Ackley, "Passive Microwave In Situ Observations of Winter Weddell Sea Ice," *J. Geophy. Res.*, **94(C8)**, 10891-10905, 1989.

Comiso, J. C, T. C. Grenfell, M. Lange, A. Lohanick, R. Moore, and P. Wadhams, "Microwave remote sensing of the Southern Ocean Ice Cover," Chapter 12, *Microwave Remote Sensing of Sea Ice,* (ed. by Frank Carsey), American Geophysical Union, Washington, D.C., 243-259, 1992.

Comiso, J. C., P. Wadhams, W. Krabill, R. Swift, J. Crawford, and W. Tucker, "Top/Bottom multisensor remote sensing of Arctic sea ice," *J. Geophy. Res.*, **96(C2)**, 2693-2711, 1991.

Emery, W. J., C. Fowler, and J. Maslanik, "Arctic sea ice concentrations from special sensor microwave imager and advanced very high resolution radiometer satellite data," *J. Geophys. Res.*, **90(C9)**, 18,329-18,342, 1994.

Gloersen, P., and D. J. Cavalieri, "Reduction of weather effects in the calculation of sea ice concentration from microwave radiances," *J. Geophys. Res.*, **91(C3)**, 3913-3919, 1986.

Gloersen P., W. J. Campbell, D. J. Cavalieri, J. C. Comiso, C. L. Parkinson, H. J. Zwally, *Arctic and Antarctic Sea Ice, 1978-1987: Satellite Passive Microwave Observations and Analysis*, **NASA SP-511**, 1992.

Grenfell, T., and J. C. Comiso, "Multifrequency Passive Microwave Observations of First Year Sea Ice Grown in a Tank," *IEEE Trans. on Geos. and Rem. Sensing*, **GE-24**, 826-831, 1986.

Grenfell, T. and A. W. Lohanick, "Temporal variations of the microwave signatures of sea ice during the late spring and early summer near Mould Bay, NWT," *J. Geophys. Res.*, **90(C3)**, 5063, 1985.

Matzler, C., R. O. Ramseier, and E. Svendsen, "Polarization effects in sea ice signatures," *IEEE J. Oceanic Engineering*, **OE-9**, 333-338, 1984.

Parkinson, C. L., J. C. Comiso, H. J. Zwally, D. J. Cavalieri, P. Gloersen, and W. J. Campbell, *Arctic Sea Ice 1973-1976 from Satellite Passive Microwave Observations*, **NASA SP-489**, 1987.

Steffen, K., D. J. Cavalieri, J. C. Comiso, K. St. Germain, P. Gloersen, J. Key, and I. Rubinstein, "The estimation of geophysical parameters using Passive Microwave Algorithms," Chapter 10, *Microwave Remote Sensing of Sea Ice*, (Frank Carsey, ed.), American Geophysical Union, Washington, D.C., 201-231, 1992.

Svendsen, E., K. Kloster, B. Farrelly, O. M. Johannessen, J. A. Johannessen, W. J. Campbell, P. Gloersen, D. Cavalieri, and C. Matzler, "Norwegian Remote Sensing Experiment: Evaluation of the Nimbus 7 Scanning multichannel microwave radiometer for sea ice research," *J. Geophys. Res.*, **88(C5)**, 2755-2769, 1983.

Swift, C. T., L. S. Fedor, and R. O. Ramseier, "An algorithm to measure sea ice concentration with microwave radiometers," *J. Geophys. Res.*, **90(C1)**, 1087-1099, 1985.

Tucker, W. B. III, D. K. Perovich, A. J. Gow, W. F. Weeks, and M. R. Drinkwater, "Physical properties of sea ice relevant to remote sensing," Chapter 2, *Microwave Remote Sensing of Sea Ice,* (ed. by Frank Carsey), American Geophysical Union, Washington, D.C., 9-28, 1992.

Wadhams, P., M. A. Lange, and S. F. Ackley, "The ice thickness distribution across the Atlantic sector of the Antarctic ocean in midwinter," *J. Geophys. Res.*, **92(C13)**, 14,535-14,552, 1987.

Zwally, H. J., J. C. Comiso, C. L. Parkinson, W. J. Campbell, F. D. Carsey, and P. Gloersen, "Antarctic Sea Ice 1973-1976 from Satellite Passive Microwave Observations," *NASA Spec. Publ.* **459**, 1983.

6. LIST OF FIGURES

Figure 10. Scatter plot illustrating the difficulty of eliminating unphysical ice concentration at the ocean/land boundaries. The symbol x represents areas at the ocean/land boundaries.

Figure 11. Scatter plot of P3 Aircraft radiometer data in the Arctic on May 20, 1987, using (a) 37H vs. 37V channels and (b) 18V vs. 37V channels. Most of the data points along the lines AD have been confirmed to represent 100% ice cover using SAR, photography, and visual observations from the aircraft.

Figure 12. Snow-ice interface and surface air temperatures for (a) sites 1 to 4 and (b) sites 5 to 8 during the 1989 Winter Weddell Gyre Experiment (courtesy of M. Lange).

Figure 13. Scatter plot of 19 GHz vs. 37 GHz (vertical polarization) in the entire Antarctic region on (a) May 11, 1992 and (b) September 14, 1992.

Figure 14. Coded-ice-concentration maps for data above the line AD-10 K in Figure 11 on (a) May 11, 1992, and (b) September 14, 1992.

Figure 15. Scatter plots of the V1937 set of the exterior and interior portions of the ice pack on September 14, 1992, for (a) exterior Weddell Sea, b) interior Weddell Sea, (c) exterior Ross/Amundsen/Bellingshausen Seas, and (d) interior Ross/Amundsen/Bellingshausen Seas.

Figure 16. Frequency histograms of ice concentration from the entire Antarctic region on (a) May 11, 1992, and (b) September 14, 1992.

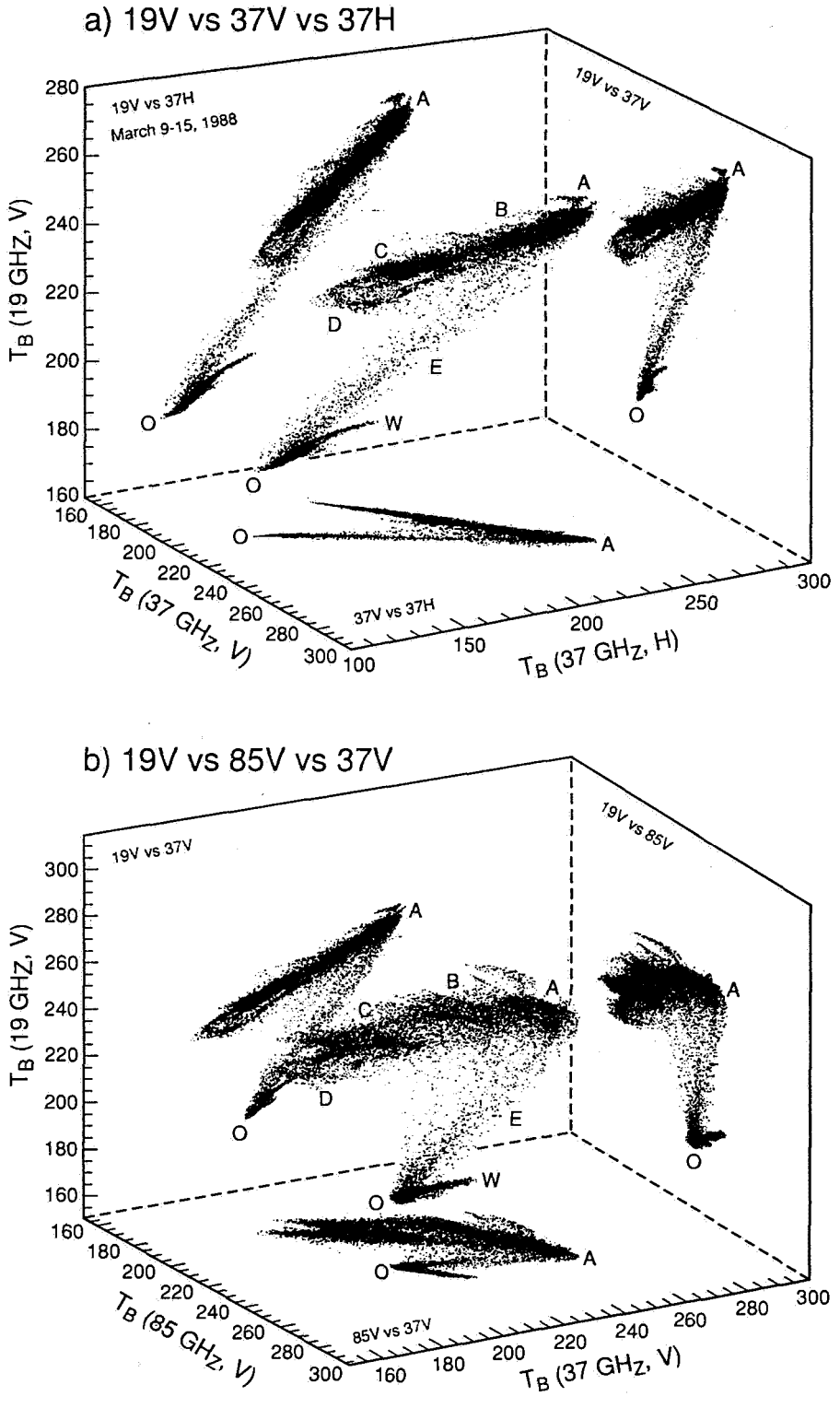

Figure 1. 3-D scatter plots of SSM/I brightness temperature data using (a) 19V vs. 37V vs. 37H and (b) 19V vs. 85V vs. 37V.

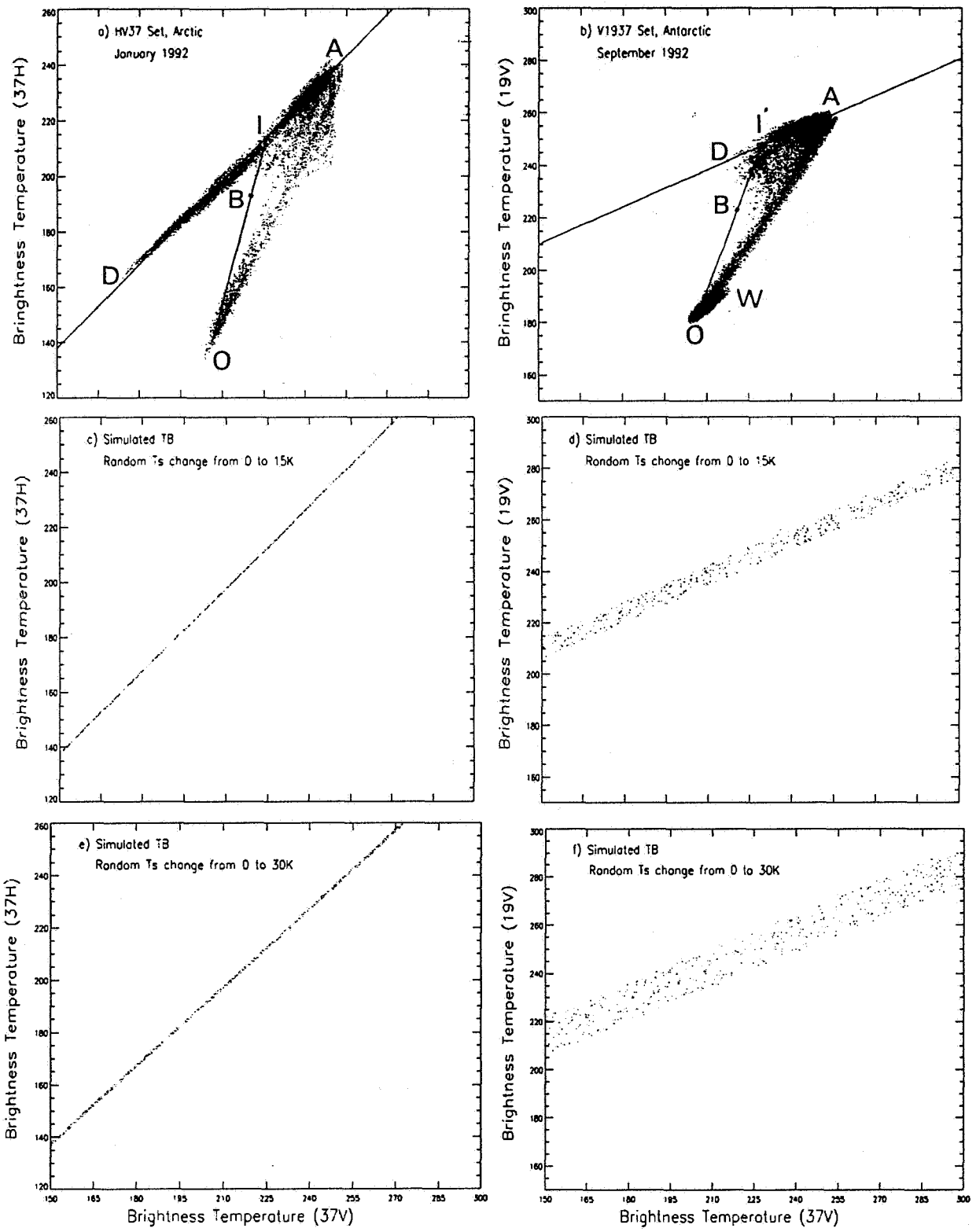

Figure 2. (a) Scatter plot of 37V vs. 37H using SMMR data; (b) sensitivity studies of the effect of randomly changing the temperature by as much as 15 K; and (c) sensitivity studies of the effect of randomly changing the temperature by 30 K; (d-e) ditto, but for 19V vs. 37V.

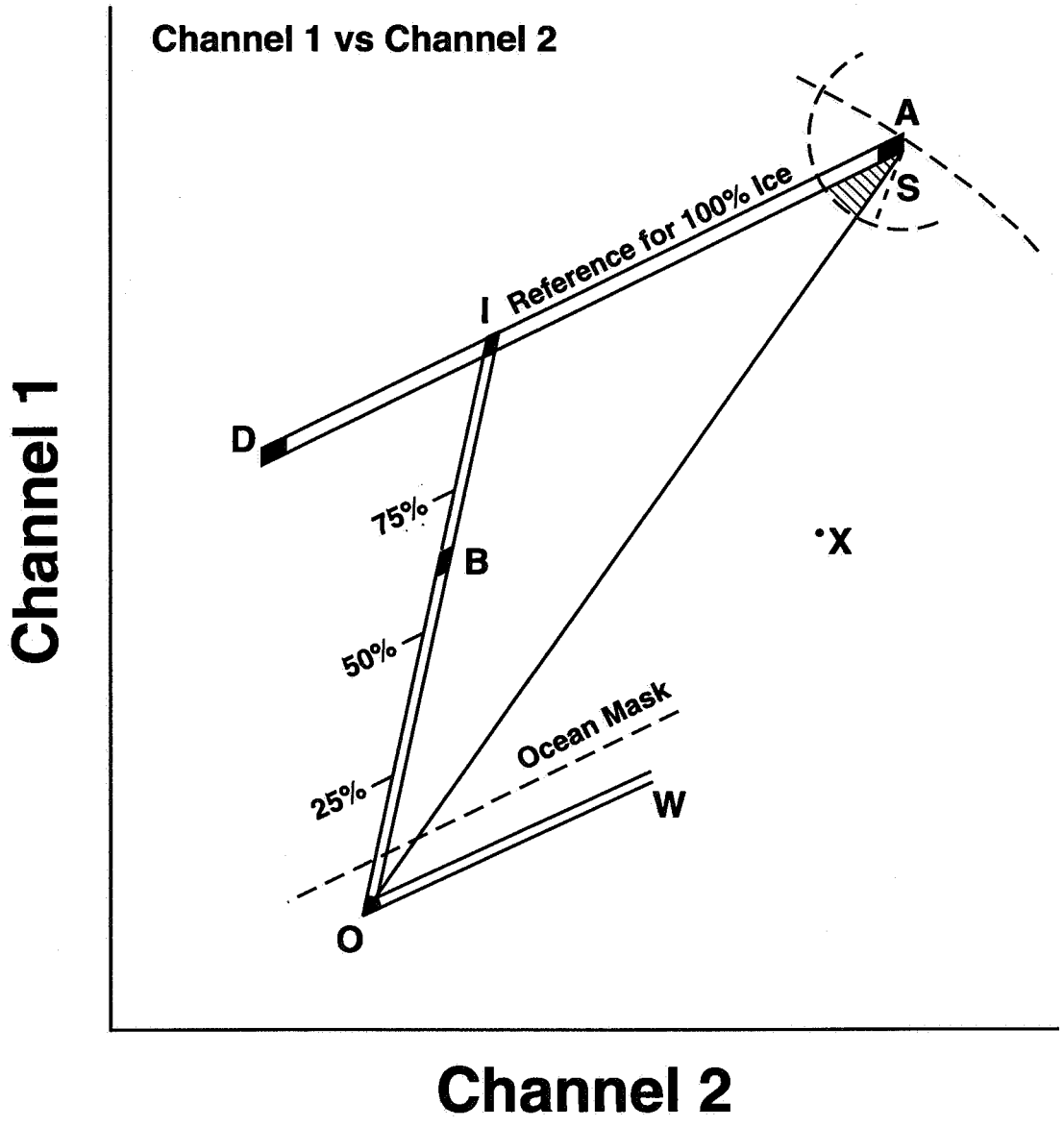

Figure 3. Schematic of the Bootstrap technique. Ice concentration at the point B is represented by OB/OI. Data points along the line AD have ice concentrations near 100%.

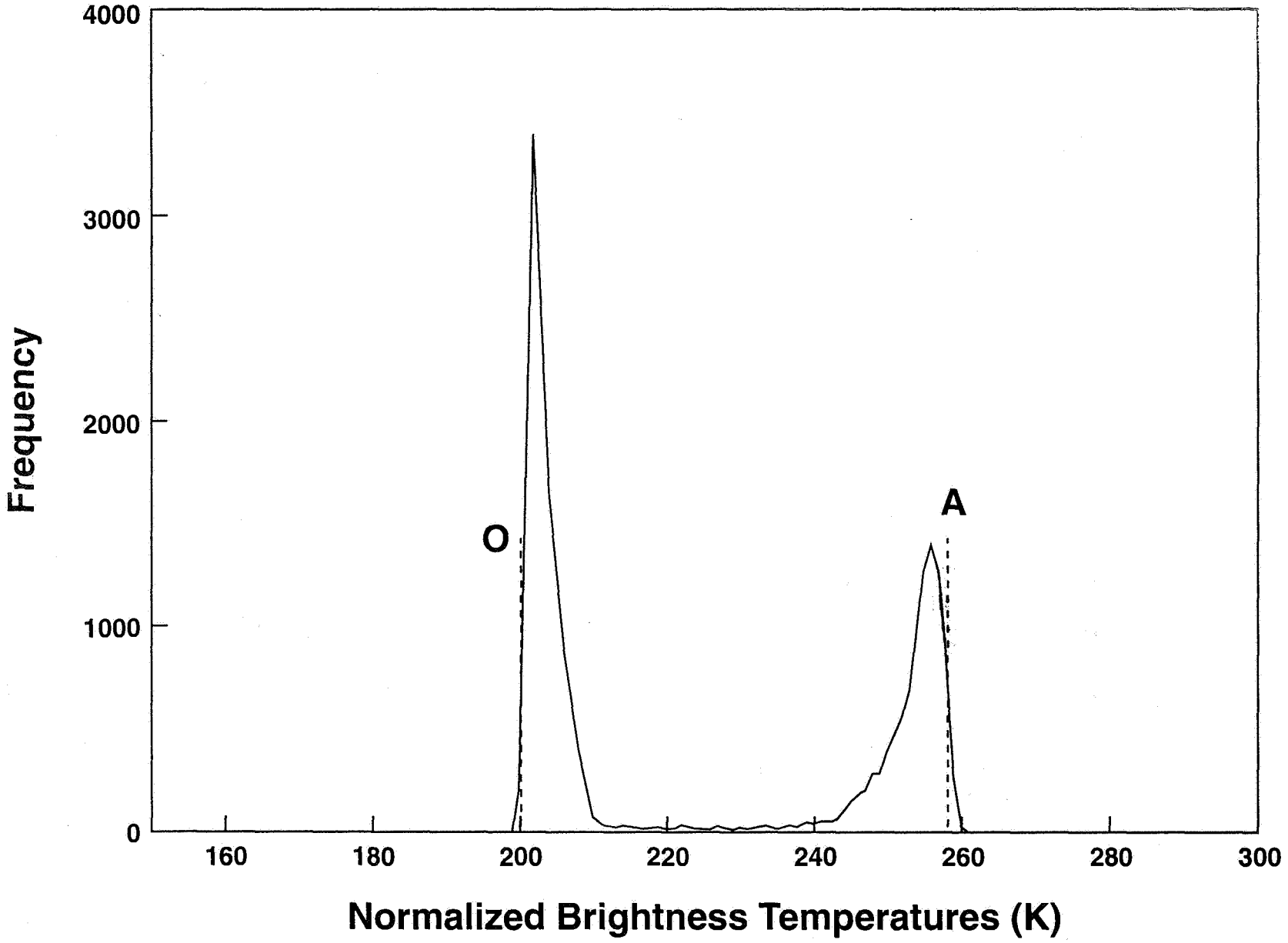

Figure 4. Histogram of brightness temperatures normalized such that the length of the line OI is constant and equal to OA.

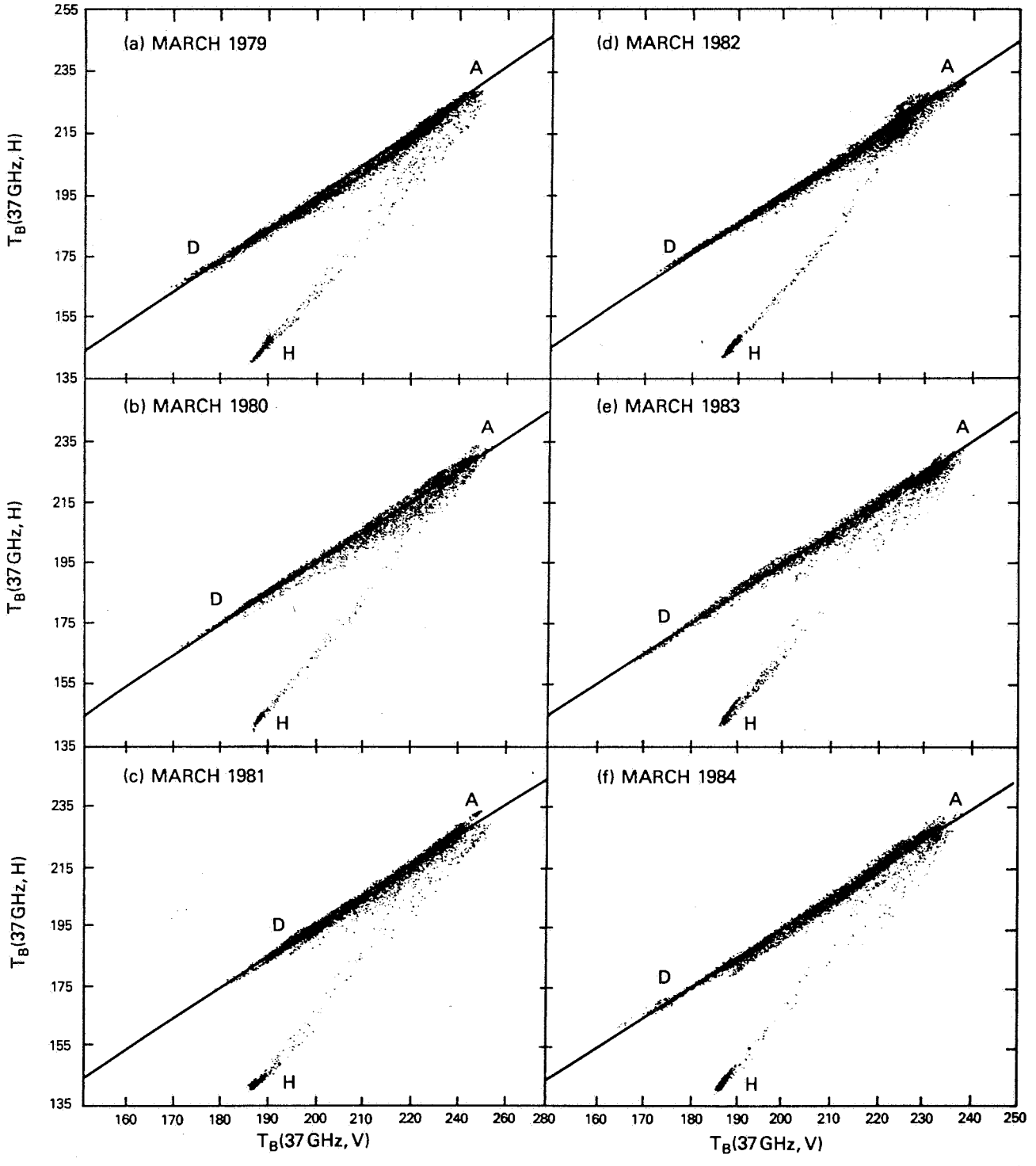

Figure 5. Scatter plots of 37H versus 37V during March of different years. The line AD is consistently drawn and can be used to indicate time consistency of the ice clusters over the SMMR years (1979-1985).

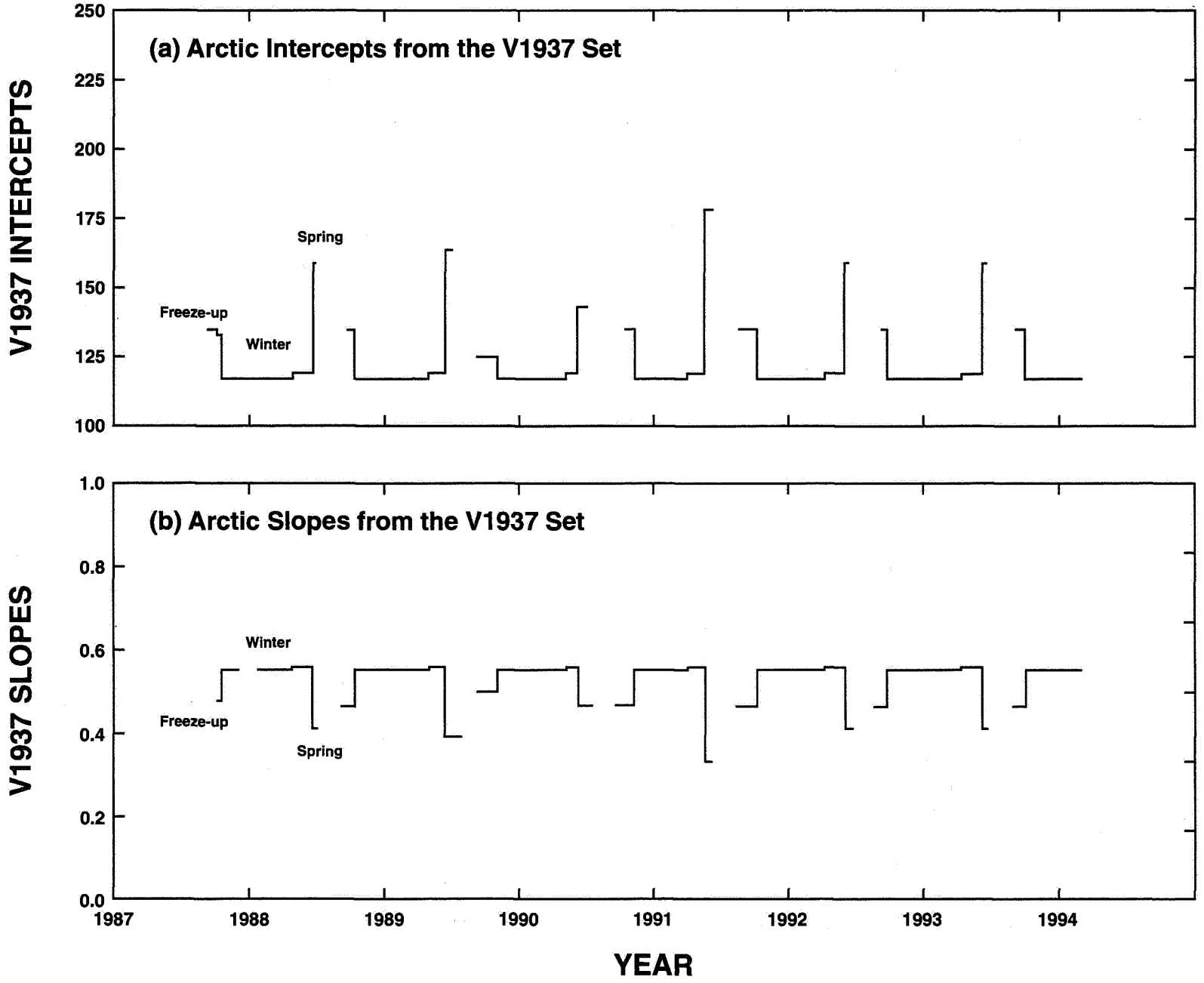

Figure 6. Plots of (a) weekly intercepts and (b) weekly slopes, in the Northern Hemisphere during winter periods from 1987 through 1994.

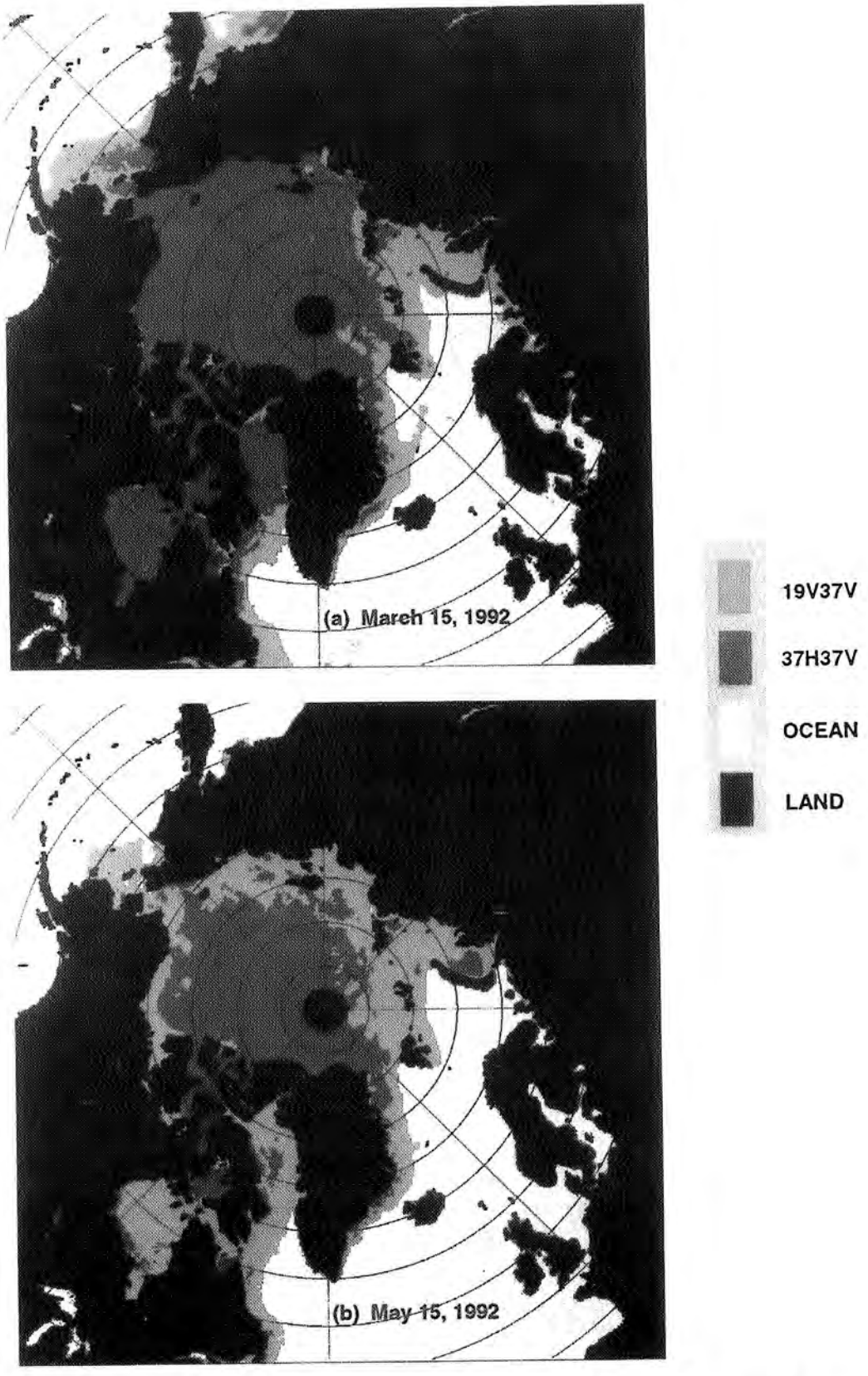

Figure 7. Maps indicating where the HV37 set is used (dark gray) compared to where V1937 set is used (light gray) on (a) March 15, 1992, and (b) June 15, 1992.

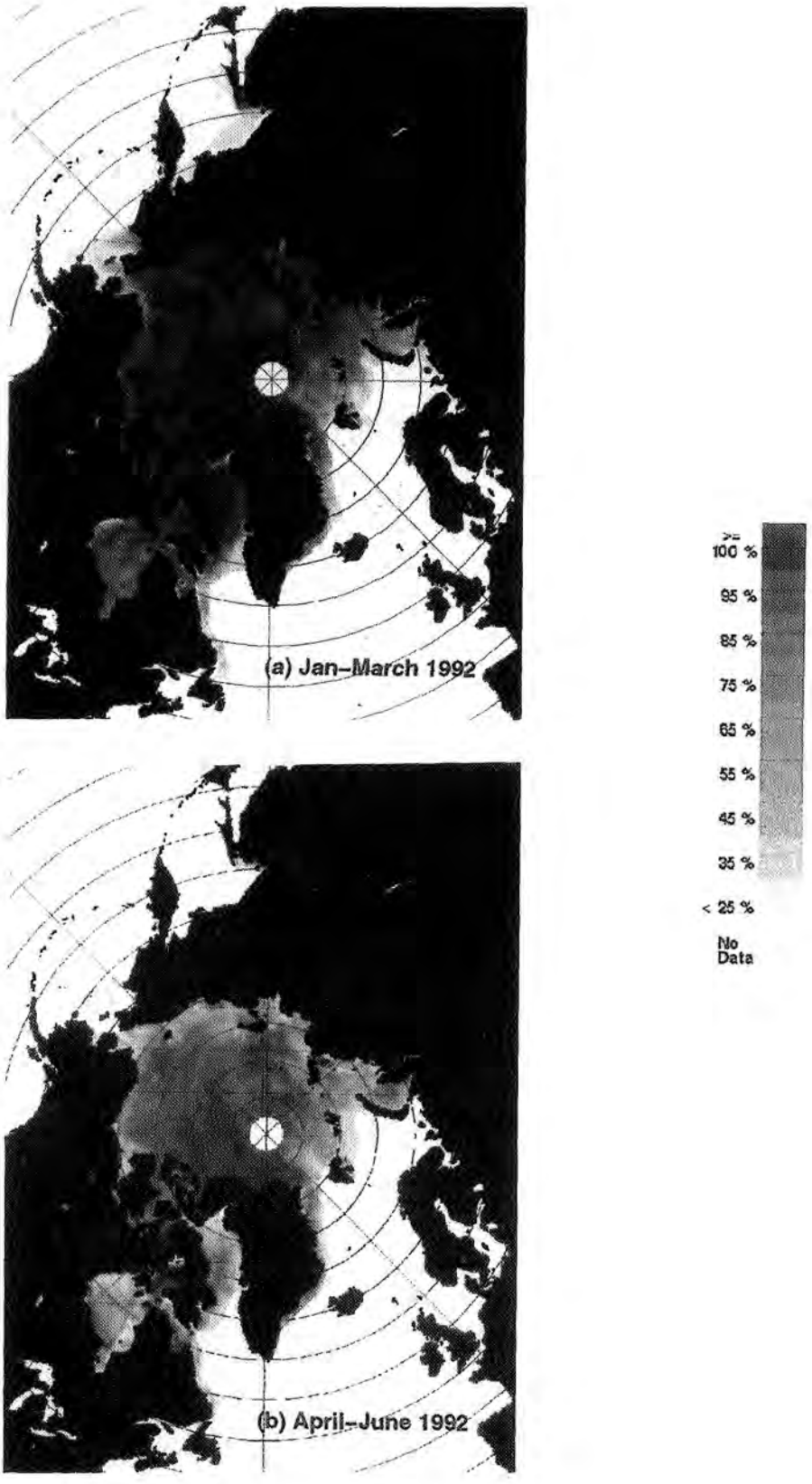

Figure 8. Map indicating the percentage of use of the HV37 set for the periods (a) January through March 1992, and (b) April through June 1992.

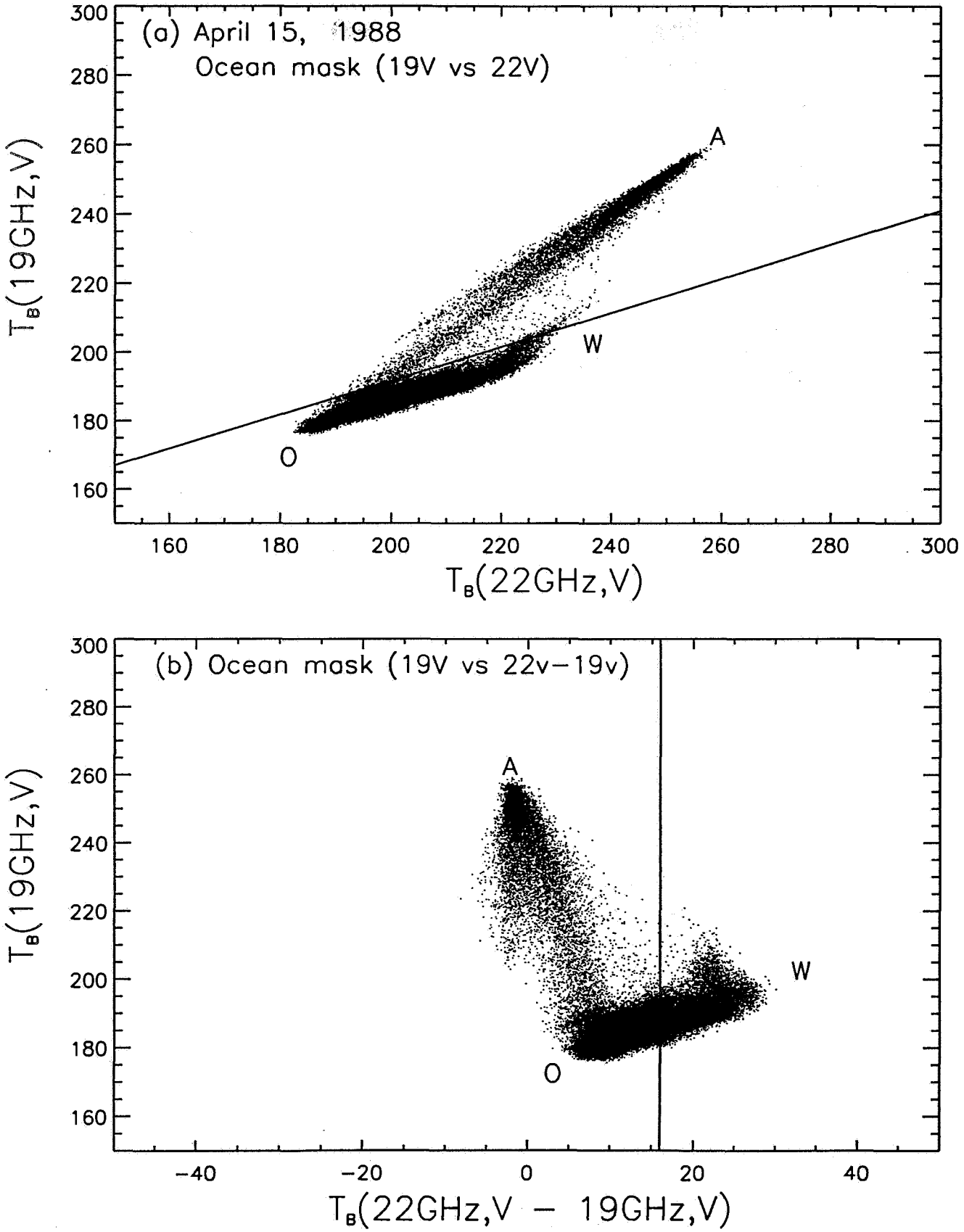

Figure 9. (a) Scatter plot of 19V vs. 22V used for ocean masking; (b) scatter plot of 19V vs. (22V-19V) illustrating how extreme conditions can be masked.

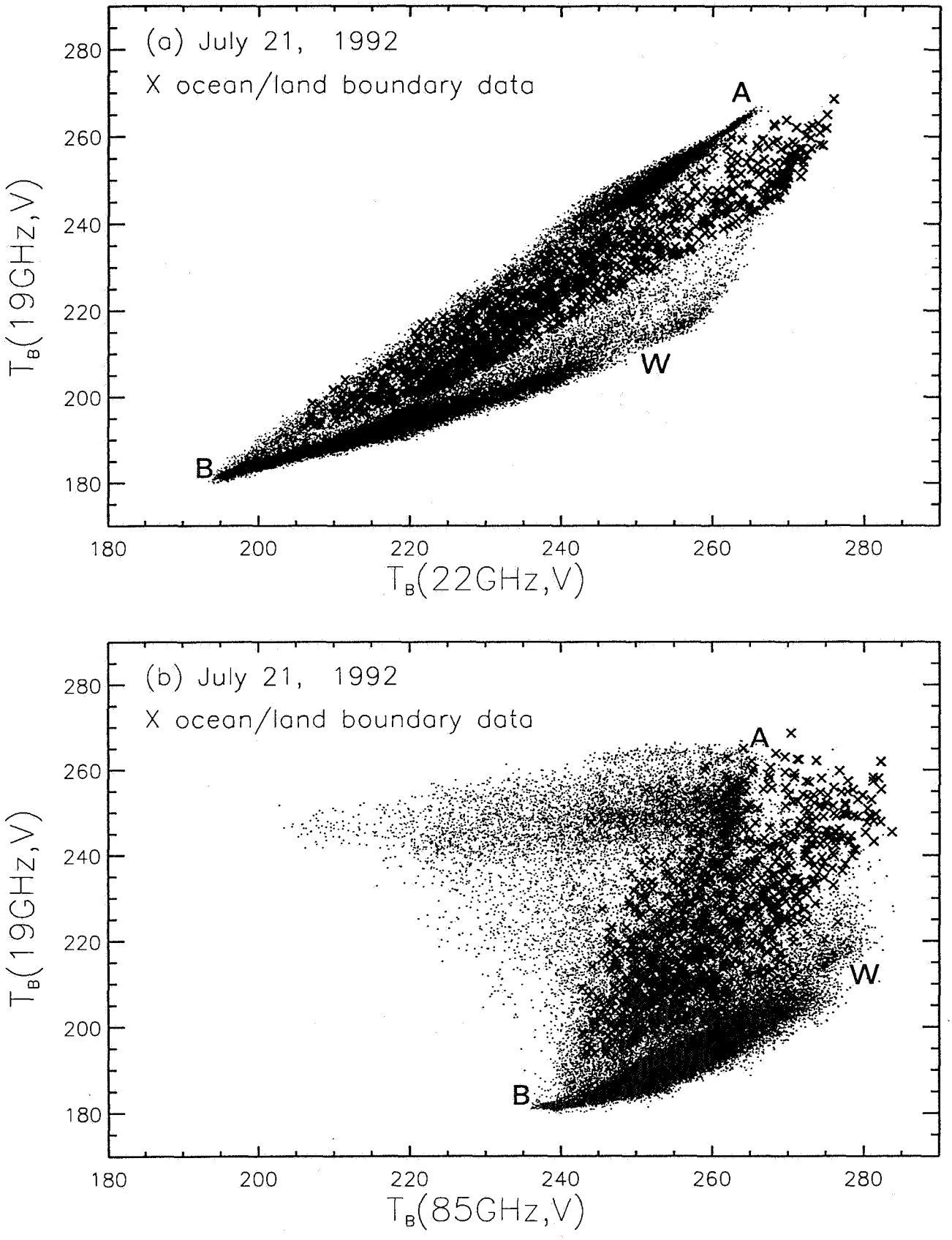

Figure 10. Scatter plot illustrating the difficulty of eliminating unphysical ice concentration at the ocean/land boundaries. The symbol x represents areas at the ocean/land boundaries.

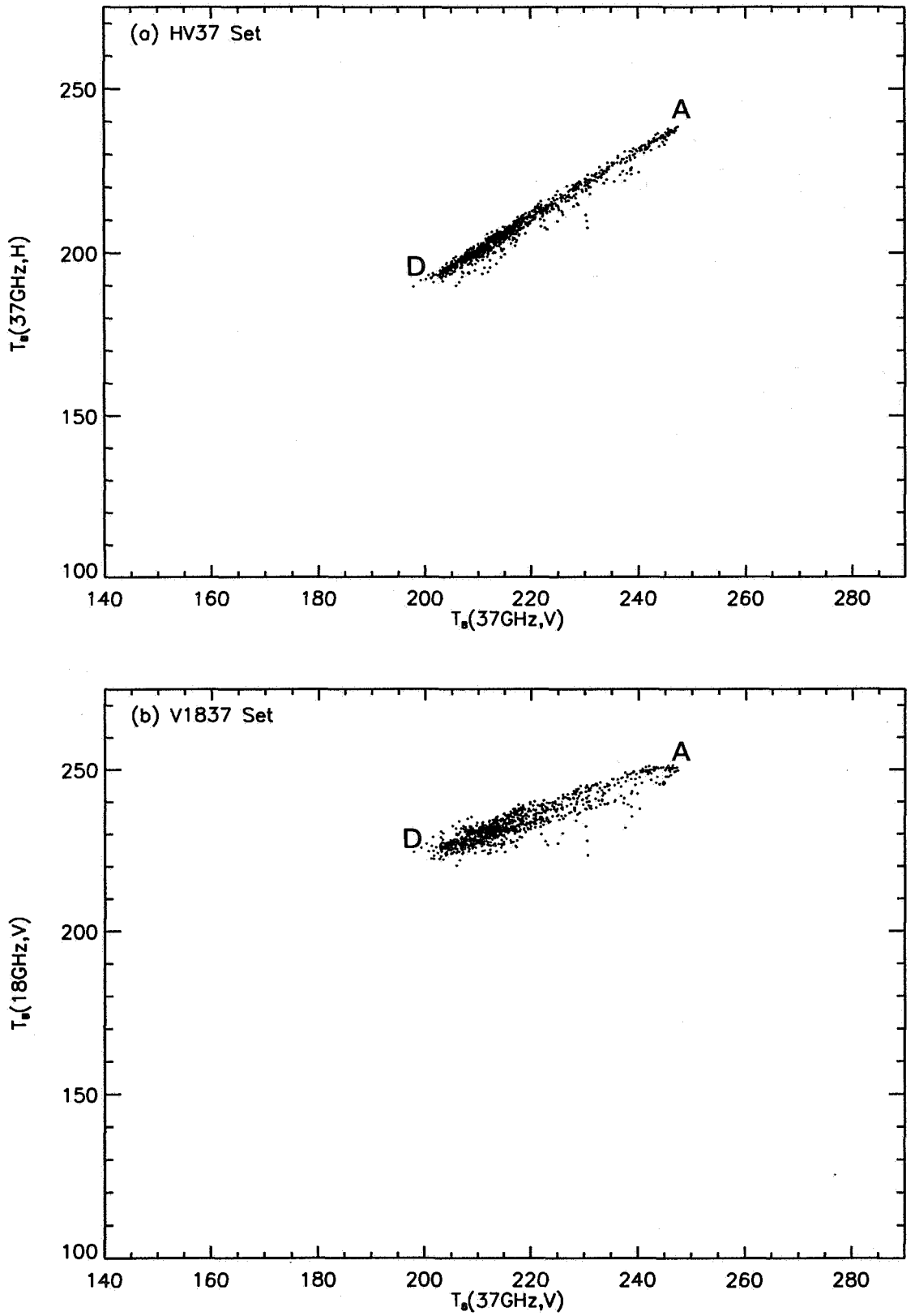

Figure 11. Scatter plot of P3 Aircraft radiometer data in the Arctic on May 20, 1987, using (a) 37H vs. 37V channels and (b) 18V vs. 37V channels. Most of the data points along the lines AD have been confirmed to represent 100% ice cover using SAR, photography, and visual observations from the aircraft.

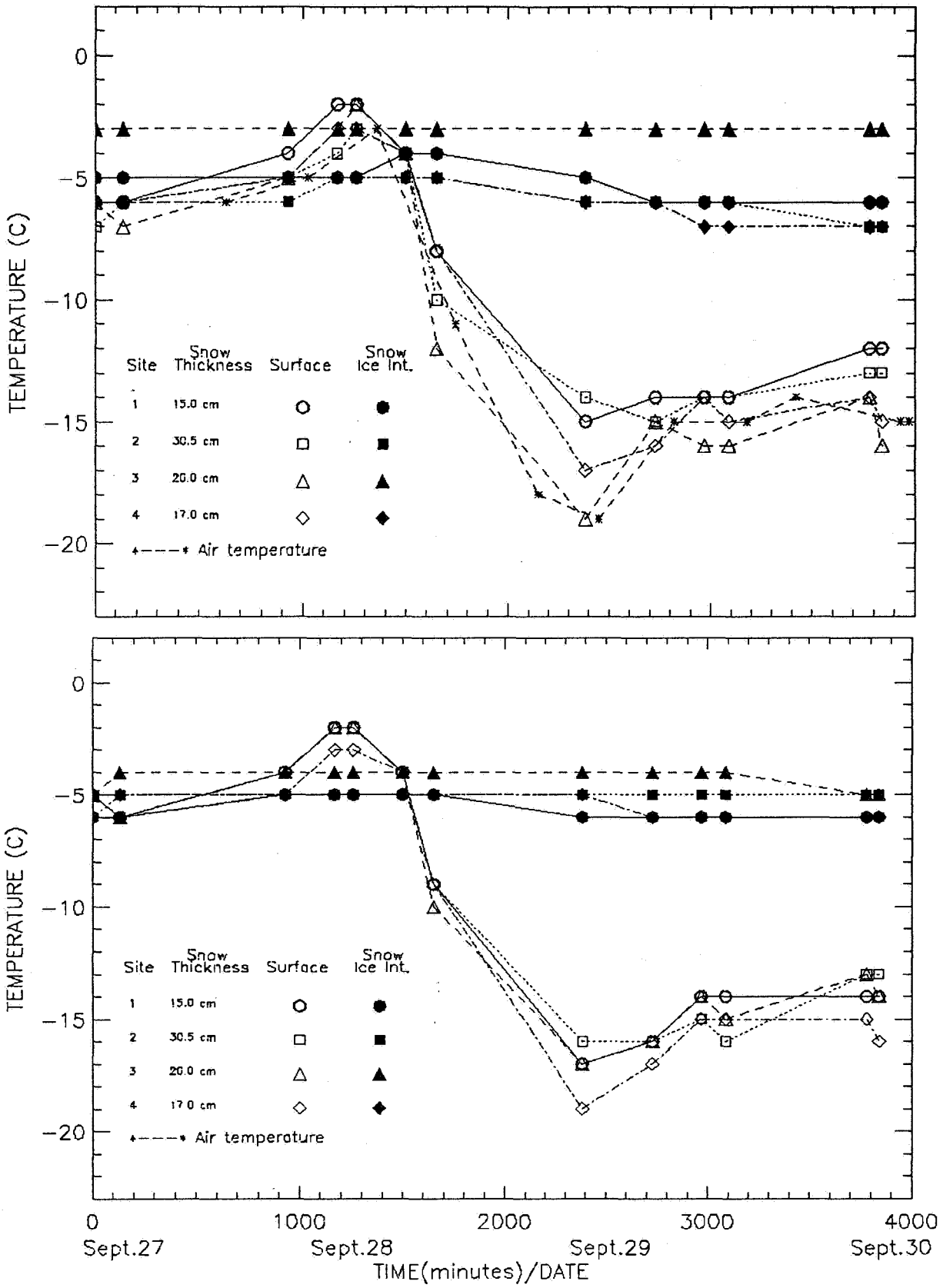

Figure 12. Snow-ice interface and surface air temperatures for (a) sites 1 to 4 and (b) sites 5 to 8 during the 1989 Weddell Winter Gyre Experiment (courtesy of M. Lange).

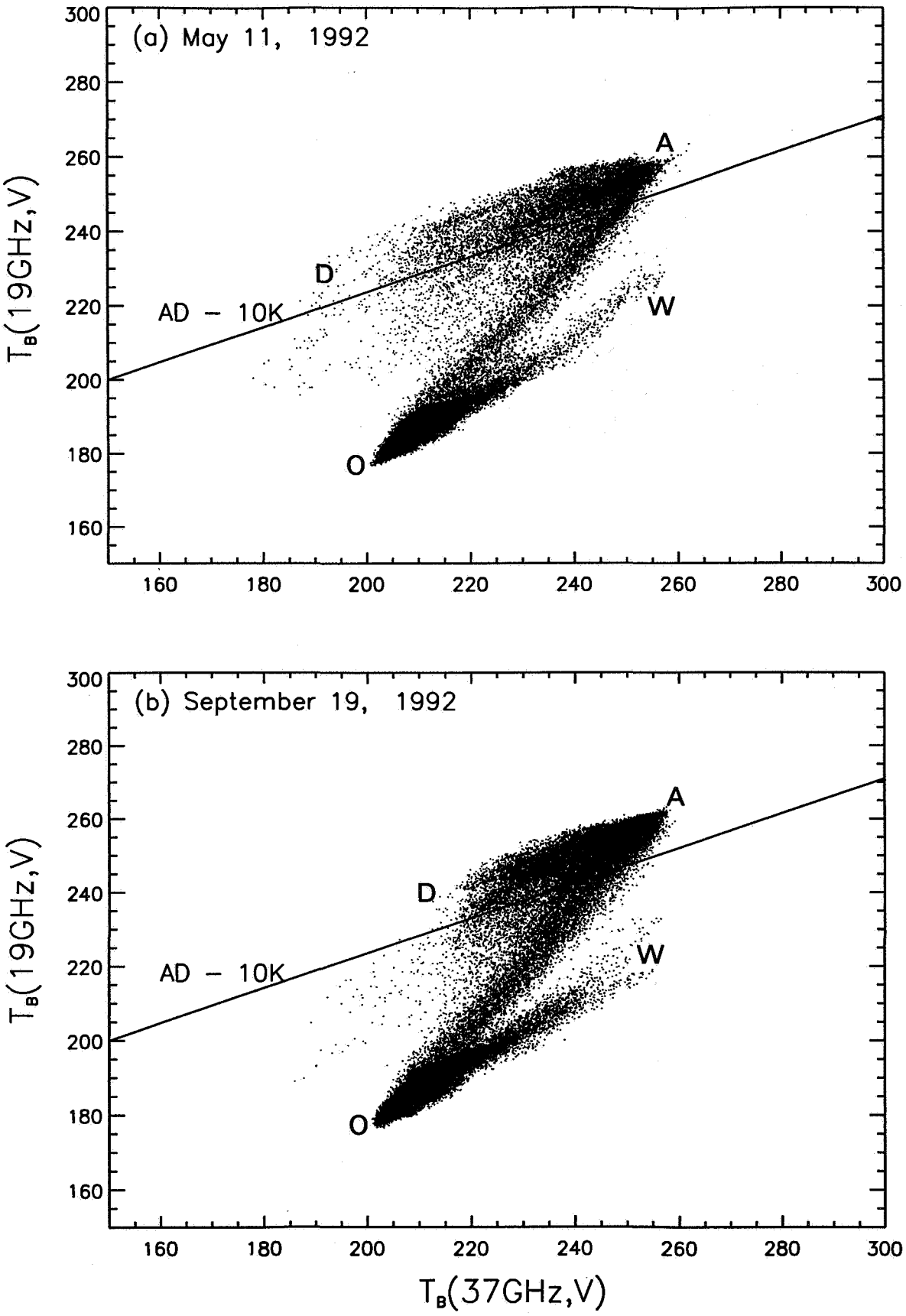

Figure 13. Scatter plot of 19 GHz vs. 37 GHz (vertical polarization) in the entire Antarctic region on (a) May 11, 1992, and (b) September 14, 1992.

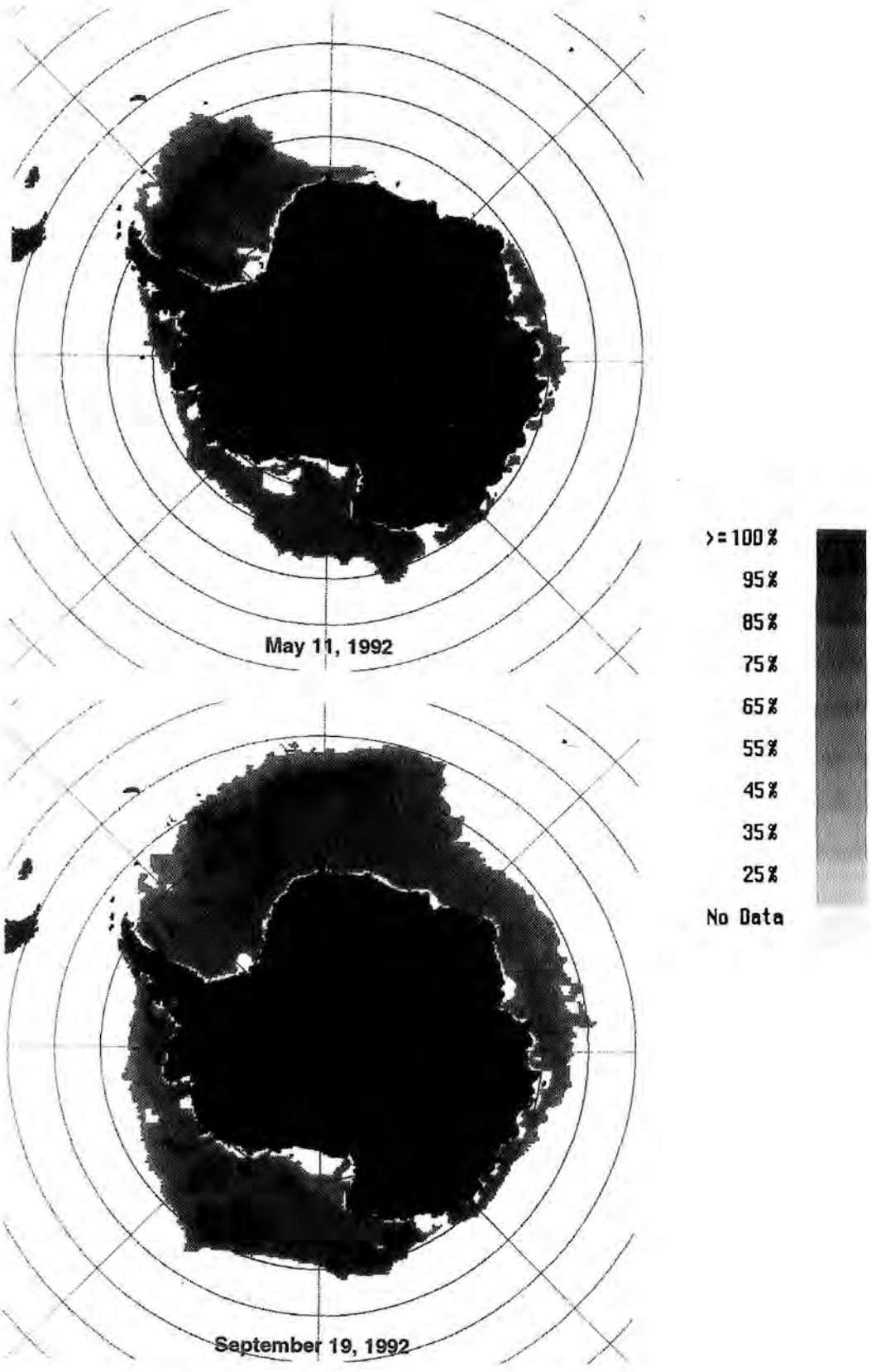

Figure 14. Coded-ice-concentration maps for data above the line AD-10K in Figure 11 on (a) May 11, 1992, and (b) September 14, 1992.

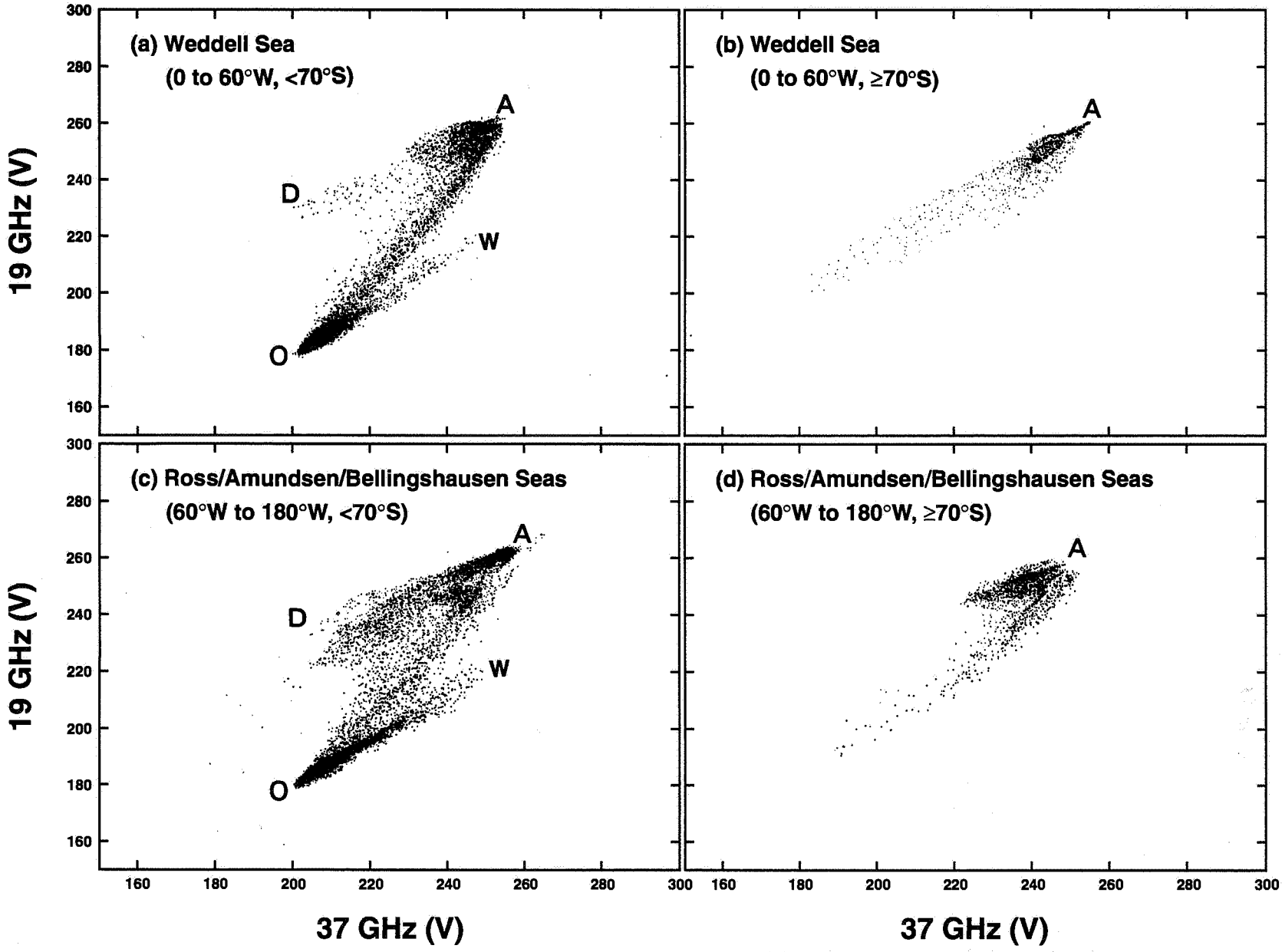

Figure 15. Scatter plots of the V1937 set of the exterior and interior portions of the ice pack on September 14, 1992 for (a) exterior Weddell Sea, (b) interior Weddell Sea, (c) exterior Ross/Amundsen/Bellingshausen Seas, and (d) interior Ross/Amundsen/ Bellingshausen Seas.

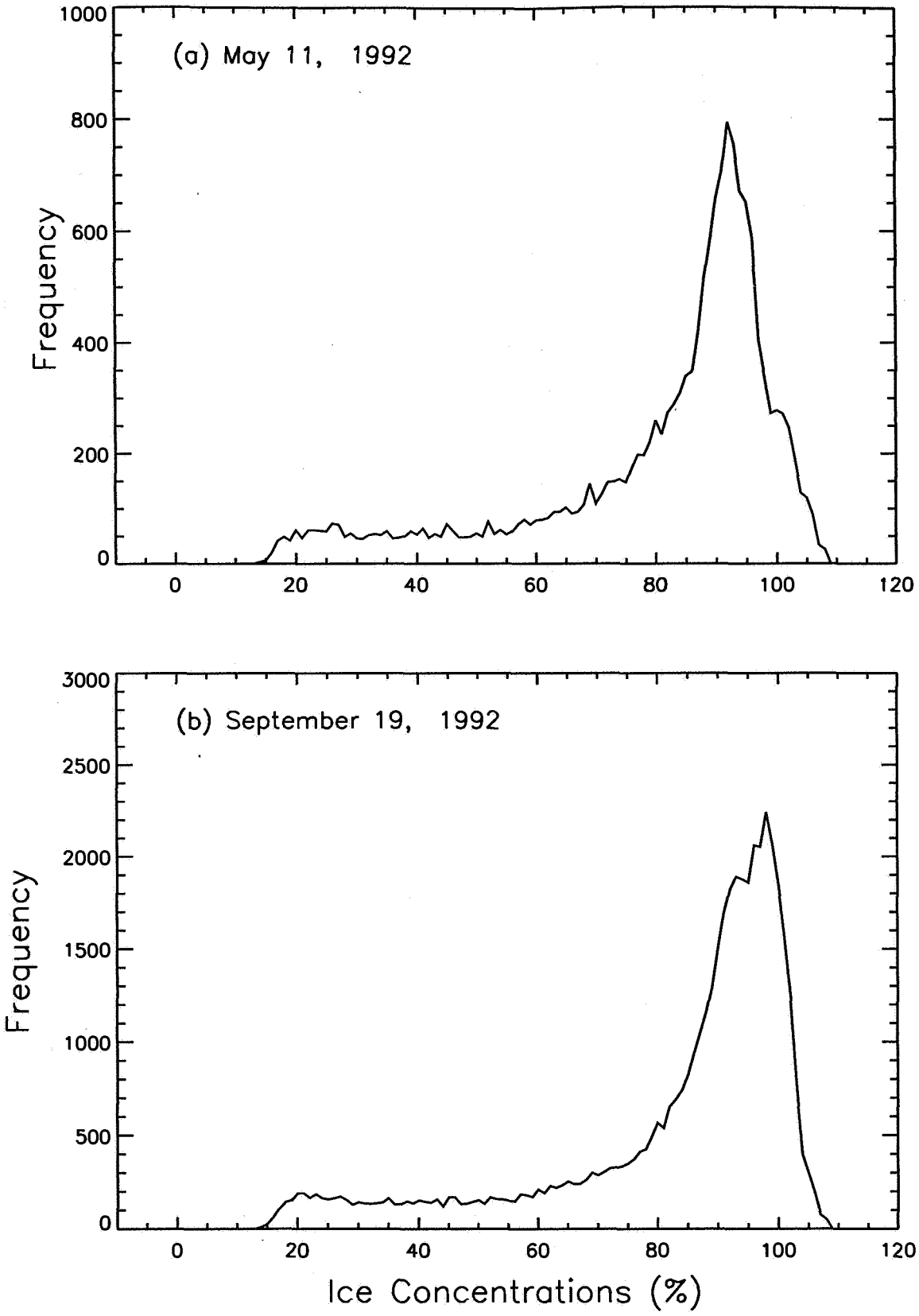

Figure 16. Frequency histograms of ice concencentrations from the entire Antarctic region on (a) May 11, 1992, and (b) September 14, 1992.

7. LIST OF TABLES

Table 1. Slopes and Offsets used by the Bootstrap Algorithm for SSM/I Data (Current Values)

	Months	Slope β	Offset α	M_0
1. 100% ice for Winter (cold) Conditions				
N.H. (37H vs. 37V)	October - June	1.000	-12.0	
N.H. (19V vs. 37V)	October - May	0.553	117.0	
S.H. (19V vs. 37V)	March - October	0.473	139.0	
2. 100% ice for Summer (warm) Conditions*				
N.H. (37H vs. 37V)	July 1 - July 18	1.226	-12.0	
	July 19 - Aug. 4	1.033	-70.0	
	Aug. 5 - Sep. 28	0.993	-14.0	
N.H. (19V vs. 37V)	June - September	0.560	119.0	
S.H. (19V vs. 37V	November - Jan.	0.473	139.0	
	Feb - March	0.620	102.0	
3. Open Ocean Masking for Winter (cold) Conditions				
N.H. (19V vs. 22V)	October - May	0.567	78.0	
N.H. (22V - 19V)				> 14 K
S.H. (19V vs. 22V)	March - October	0.493	93.0	
S.H. (22V - 19V)				> 16 K
4. Open Ocean Masking for Summer (warm) Conditions				
N.H. (19V vs. 22V)	June - October	0.580	72.26	
N.H. (22V - 19V)				> 23 K
S.H. (19V vs. 22V)	November - Feb.	0.493	93.0	
S.H. (22V - 19V)				> 16 K
5. Open Water Tie-Points for Cold Conditions				
N.H.: 19V = 179 K, 37V = 202 K, 37H = 130 K				
S.H.: 19V = 179 K, 37V = 202 K				
6. Open Water Tie-Points for Summer Conditons				
N.H.: 19V = 181 K, 37V = 203 K, 37H = 130 K				
S.H.: 19V = 179 K, 37V = 202 K				

*The values are further refined on a daily basis using an automated system for a smooth transition between adjustment periods.

Table 2. Slopes and Offsets used by the Bootstrap Algorithm for SSM/I Data (Old Values)

	Months	Slope	Offset
1. 100% ice for Winter (cold) Conditions			
N.H. (37H vs. 37V)	October - May	1.045	-21.2
N.H. (19V vs. 37V)	October - May	0.50	132.0
S.H. (19V vs. 37V)	March - October	0.45	145.8
2. 100% ice for Summer (warm) Conditions			
N.H. (37H vs. 37V	June - September	1.045	-21.2
N.H. (19V vs. 37V)	June and July	0.22	209.5
	August	0.31	181.0
	September	0.47	138.0
S.H. (19V vs. 37V)	November - Feb.	0.38	168.0
3. Open Ocean Masking for Winter (cold) Conditions			
N.H. (19V vs. 37V)	October - May	0.80	21.5
S.H. (19V vs. 37V)	March - October	0.80	21.0
4. Open Ocean Masking for Summer (warm) Conditions			
N.H. (19V vs. 37V)	June - September	0.80	21.5
S.H. (19V vs. 37V)	November - Feb.	0.80	21.0
5. Open Water Tie Points for Cold Conditions			
N.H.: 19V = 182 K, 37V = 205 K, 37H = 141 K,			
S.H.: 19V = 182 K, 37V = 205 K			
6. Open Water Tie Points for Summer Conditons			
N.H.: 19V = 182 K, 37V = 205 K, 37H = 141 K,			
S.H.: 19V = 182 K, 37V = 205 K			

Table 3. Reference Brightness Temperatures at A

1. Northern Hemisphere

	$T_B(37V)$	$T_B(37H)$
Winter	258 K	249 K
Summer	267 K	258 K

2. Southern Ocean:

	$T_B(19V)$	$T_B(37V)$
Winter	256 K	262 K
Summer	256 K	262 K

Table 4. Bootstrap Algorithm Ice-Concentration Sensitivity to 1-K Change in the Various Parameters

	δC for C=100%		δC for C=50%	
	A+	D	A	D
HV37 (Northern Hemisphere):				
TS	0.0533	0.0533	0.0266	0.0246
T1O	0.0007	0.0014	0.0001	0.0001
T2O	0.0007	0.0014	0.0005	0.0005
T1I	0.2333	0.4688	0.1167	0.4602
T2I	0.7349	0.3460	0.3669	0.6612
dT_B(37H)	1.1765	1.1765	0.5882	0.5882
dT_B(37V)	1.1765	1.1765	0.5882	0.5882
RSS*	1.6638	1.6638	0.8318	0.8318
V1937 (Northern Hemisphere)				
TS	0.8400	0.8450	0.4200	0.4226
T1O	0.0170	0.0037	0.0174	0.0038
T2O	0.0091	0.0020	0.0090	0.0020
T1I	0.4213	0.9802	0.4185	0.9629
T2I	0.2760	0.4212	0.2762	0.4141
dT_B(19V)	1.9174	1.9174	0.9587	0.9587
dT_B(37V)	1.0603	1.0603	0.5302	0.5302
RSS*	2.1910	2.1910	1.0955	1.0955
V1937 (Southern Hemisphere)				
TS	0.9100	0.9110	0.4553	0.4554
T1O	0.0005	0.0013	0.0002	0.0006
T2O	0.0002	0.0006	0.0001	0.0001
T1I	0.8236	1.3356	0.4118	0.6678
T2I	0.5497	0.4235	0.2749	0.3669
dT_B(19V)	1.7361	1.7361	0.8680	0.8681
dT_B(37V)	0.8212	0.8212	0.4106	0.5882
RSS*	1.9205	1.9205	0.9602	0.9602

+A and D are locations of the end points of the consolidated ice cluster as shown in Figures 2 (a) and (b).
*RSS is the root-summed-square of the dT_Bs.

Table 5. Conversion of Surface-Air Temperature to Snow-Ice Interface Temperature

Air Temperature (^{0}C)	Snow-Ice Interface Temperature (^{0}C)				
	Weddell	Pond Inlet	25% Rule	55%	64%
- 5	- 4.4	-6.5	- 4.2	- 3.4	- 3.1
-10	- 5.6	-8.7	- 8.0	- 5.6	- 4.9
-15	- 6.8	-10.8	-11.8	- 7.8	- 6.7
-20	- 7.9	-13.0	-15.5	-10.1	- 8.5
-25	- 9.1	-15.1	-19.2	-12.4	-10.3
-30	-10.3	-17.3	-23.0	-14.6	-12.1
-35	-11.5	-19.4	-26.7	-16.8	-13.9
-40	-12.7	-21.6	-30.5	-19.1	-15.7
-45	-13.9	-23.7	-34.2	-21.4	-17.5

Appendix A: BASIC PROGRAM TO CALCULATE ICE CONCENTRATION

```
'The Bootstrap Ice Concentration Algorithm
'   For SSM/I Data
'   A simple one pixel program that uses data
'   from 2-channels at a time i.e., (chan 1, chan 2),
'   where channel 1 is 19v or 37h and channel 2 is 37v data.
'   Test data for the northern hemisphere:  (238.0, 250.0)
'   Test data for the southern hemisphere:  (257.2, 250.0)
'
'Input Brightness Temperatures at Study Region
'
INPUT "tb(37h or 19v)= "; t1b
INPUT "tb(37v)= ", t2b
INPUT "type = 1 for hv37, 2 for v1937"; itype
'Input the Hemisphere
INPUT "hemis=1 for NH, 2 for SH"; ihem
IF ihem = 2 THEN 30
IF itype = 2 THEN 25
'  Input data for the hv37 set, northern hemisphere
sad = 1!
t1a = -12!
t2a = 0
t20 = 202!
t10 = 130!
GOTO 35
'   Input data for the v1937 set, northern hemisphere
25  t1a = 117!
    t2a = 0!
    sad = .553
    t20 = 202!
    t10 = 179!
    GOTO 35
    '   Input data for the v1937 set, southern hemisphere
30  t1a = 139!
    t2a = 0!
    sad = .473
    t20 = 202!
    t10 = 179!
    '   Determine ice reference temperatures
35  sob = (t1b - t10) / (t2b - t20)
    t2i = (t1a - t10 - t2a * sad + t20 * sob) / (sob - sad)
    t1i = sob * t2i + t10 - t20 * sob
    PRINT "intercepts ="; t1i, t2i
    '
    ' Calculate the Ice Concentration
    c1 = (t1b - t10) ^ 2 + (t2b - t20) ^ 2
    c2 = (t1i - t10) ^ 2 + (t2i - t20) ^ 2
    c = SQR(c1 / c2)
    PRINT "ice concentration  ="; c
    END
```

REPORT DOCUMENTATION PAGE

Form Approved
OMB No. 0704-0188

1. AGENCY USE ONLY *(Leave blank)*	2. REPORT DATE	3. REPORT TYPE AND DATES COVERED
	December 1995	Reference Publication

4. TITLE AND SUBTITLE

SSM/I Sea Ice Concentrations Using the Bootstrap Algorithm

5. FUNDING NUMBERS

Code 971

6. AUTHOR(S)

Josefino C. Comiso

7. PERFORMING ORGANIZATION NAME(S) AND ADDRESS (ES)

Laboratory for Hydrospheric Processes
Goddard Space Flight Center
Greenbelt, Maryland 20771

8. PEFORMING ORGANIZATION REPORT NUMBER

96B00013

9. SPONSORING / MONITORING AGENCY NAME(S) AND ADDRESS (ES)

National Aeronautics and Space Administration
Washington, DC 20546-0001

10. SPONSORING / MONITORING AGENCY REPORT NUMBER

NASA RP-1380

11. SUPPLEMENTARY NOTES

Comiso: Goddard Space Flight Center, Greenbelt, Maryland 20771

12a. DISTRIBUTION / AVAILABILITY STATEMENT

Unclassified - Unlimited
Subject Category 48

Availability: NASA CASI (301) 621-0390.

12b. DISTRIBUTION CODE

13. ABSTRACT *(Maximum 200 words)*

A detailed description of the Bootstrap algorithm for sea ice, as discussed previously in earlier publications, is presented. The algorithm was developed initially for the Nimnbus-7 SMMR data and has been enhanced to make it more suitable for the SSM/I data. The technique utilizes relationships of multichannel distributions of the data to derive geophysical parameters. The physical basis for the formulation is presented and shown to be consistent with microwave observations from ships and aircrafts. Two modes of retrievals are used: one using the 37-GHz channels at both polarizations, and another using the 19-GHz channels at vertical polarization. The first is used primarily in the Arctic region and provides statistical uncertainties of less than 5%. The second is used primarily in the Antarctic and some of the seasonal regions of the Arctic. The statistical uncertainty in the latter region is about 10% and is greater than the first, because it does not account for spatial changes in physical temperatures of the emitting ice layer as well. Large variabilities in emissivity, and meltponding effect during the summer, further degrade the accuracy to about 20% to 25% in some regions. The algorithm provides ice-concentration values that are coherent spatially and temporally. The product is generally useful for large-scale studies of the ice cover because of consistent retrieval at good temporal resolution.

14. SUBJECT TERMS

Algorithm, sea ice

15. NUMBER OF PAGES

57

16. PRICE CODE

17. SECURITY CLASSIFICATION OF REPORT	18. SECURITY CLASSIFICATION OF THIS PAGE	19. SECURITY CLASSIFICATION OF ABSTRACT	20. LIMITATION OF ABSTRACT
Unclassified	Unclassified	Unclassified	UL